This is a repository copy of *TiO2/Cu2O/CuO Multi-Nanolayers as Sensors for H2 and Volatile Organic Compounds: An Experimental and Theoretical Investigation*.

White Rose Research Online URL for this paper:
https://eprints.whiterose.ac.uk/175369/

Version: Supplemental Material

Supporting Information

S-1

TiO$_2$/Cu$_2$O/CuO Multi-Nanolayers as Sensors for H$_2$ and Volatile Organic Compounds: An Experimental and Theoretical Investigation

Oleg Lupan,[1,2,3,*] David Santos-Carballal,[4,*] Nicolai Ababii,[2] Nicolae Magariu,[2] Sandra

Hansen,[1,*] Alexander Vahl,[5] Lukas Zimoch,[1] Mathias Hoppe,[1] Thierry Pauporte,[6] Vardan

Galstyan,[7] Victor Sontea,[8,9] Lee Chow,[3] Franz Faupel,[5,*] Rainer Adelung,[1,*] Nora H de

Leeuw,[4,10] Elisabetta Comini[7]

[1] *Functional Nanomaterials, Faculty of Engineering, Institute for Materials Science, Kiel University, Kaiserstr. 2, D-24143, Kiel, Germany*
[2] *Center for Nanotechnology and Nanosensors, Technical University of Moldova, 168 Stefan cel Mare Av., MD-2004 Chisinau, Republic of Moldova*
[3] *Department of Physics, University of Central Florida, Orlando, FL 32816-2385, USA*
[4] *School of Chemistry, University of Leeds, Leeds LS2 9JT, United Kingdom*
[5] *Faculty of Engineering, Chair for Multicomponent Materials, Christian-Albrechts Universität zu Kiel, str. Kaiserstraße nr. 2, D-24143, 16 Kiel, Germany*
[6] *Institut de Recherche de Chimie Paris-IRCP, Chimie ParisTech, PSL Université, rue Pierre et Marie Curie 11, 75231 Paris Cedex 05, France*
[7] *Sensor Laboratory, Department of Information Engineering (DII), University of Brescia, Via Valotti 9, 25133 Brescia, Italy*
[8] *National Center for Biomedical Engineering, Technical University of Moldova, 168 Stefan cel Mare Av., MD-2004 Chisinau, Republic of Moldova*
[9] *Department of Nanoelectronics and Surface Modification, Sumy State University, 2, Rymskogo-Korsakova Str., 40007 Sumy, Ukraine*
[10] *Department of Earth Sciences, Utrecht University, Budapestlaan 4, 3584 CD Utrecht, The Netherlands*

[*]Corresponding authors:
Prof. Dr. O. Lupan, (ollu@tf.uni-kiel.de ; oleg.lupan@mib.utm.md)
Kiel University, Germany; Technical University of Moldova, Moldova; UCF, U.S.A.

Prof. Dr. R. Adelung, (ra@tf.uni-kiel.de)
Kiel University, Germany

Dr. S. Hansen, (sn@tf.uni-kiel.de)
Kiel University, Germany

Prof. Dr. F. Faupel, (ff@tf.uni-kiel.de)
Kiel University, Germany

Dr. David Santos-Carballal (d.santos-carballal@leeds.ac.uk)
University of Leeds, United Kingdom.

Supporting Information Text S1

The surface properties of the binary and ternary heteroepitaxial interfaces were simulated using spin-polarised density functional theory (DFT) calculations as implemented within the Vienna ab-initio simulation package (VASP) [1–4]. We have used the generalised gradient approximation (GGA) functional of Perdew, Burke and Ernzerhof (PBE) for the exchange-correlation energy [5]. The projector augmented wave (PAW) method was employed to model the atomic frozen core electrons and their interaction with the valence states [6,7]. The core electrons included [Ne] $3s^2$ for Cu; [Ne] for Ti; and [He] for O, C and N. For the H atom, the electron was treated as valence. The kinetic energy cut-off was set at 400 eV for the expansion of the periodic plane wave basis set. Long-range dispersion interactions were considered using the semi-empirical method of Grimme, with the Becke-Johnson damping [D3-(BJ)] [8,9], which is important to describe properly the bulk and surface properties of a range of materials [10–18]. The optimization of the structures was conducted *via* an efficient force-based conjugate-gradients method that uses a Newton's line optimizer [19,20], which stopped when the Hellmann-Feynman forces on all atoms were smaller than 0.01 eV·Å^{-1}. We have used the Dudarev *et al.*[21] approach within the DFT+U framework [22] to describe the d electrons in the metal oxide phases. The values for the on-site Coulomb interaction term in this study were U_{eff} = 4.0 eV for Cu and 4.4 eV for Ti [23–27]. These criteria allowed convergence of the total electronic energy to within 1 meV atom^{-1}.

The electronic integrations of the bulk phases were performed in the reciprocal space using their primitive unit cells and a Γ-centred Monkhorst-Pack sampling grid [28] containing 11 × 11 × 11 k-points for Cu_2O as well as TiO_2, and 14 × 14 × 8 k-points for CuO. This choice of mesh density was found to be enough to predict correctly the insulating electronic properties of the metal oxide phases [29–33]. The heteroepitaxial interfaces were modelled using the commensurate 5 × 5 × 1 k-points mesh, whereas the isolated molecules were simulated in a cell with broken symmetry and a volume of 9240 Å^3, sampling only the Γ point of the Brillouin zone. For the isolated molecules,

the electronic partial occupancies were determined using the Gaussian smearing method with a width of the smearing of 0.05 eV. We tested several values for the width of the smearing, to ensure that the electronic entropy was negligible, which is the variational quantity of these partial occupancies methods [34]. However, the tetrahedron method with Blöchl corrections [35] was used for the oxides and for the calculation of the electronic and magnetic properties and to obtain very accurate total energies.

The adsorption energy of the molecule is calculated as follows:

$$E_{ads} = E_{surf+mol} - (E_{surf} + E_{mol}), \tag{S1}$$

where $E_{surf+mol}$ is the total energy of the adsorbate–substrate system, E_{surf} is the energy of the naked surface slab, and E_{mol} is the energy of the isolated molecule.
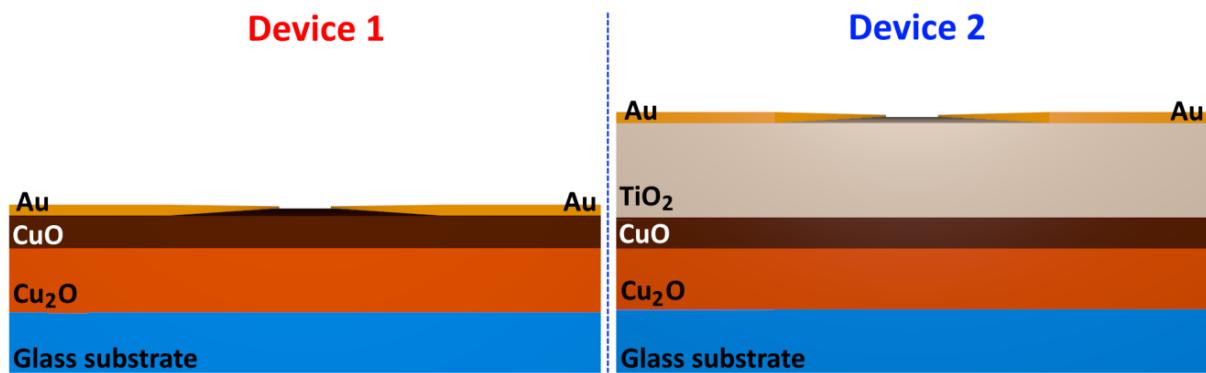
Figure S1. Cross-section view of set #1 devices made from CuO/Cu_2O nanolayers (Device 1), and set #2 based on $TiO_2/CuO/Cu_2O$ heterolayers (Device 2).
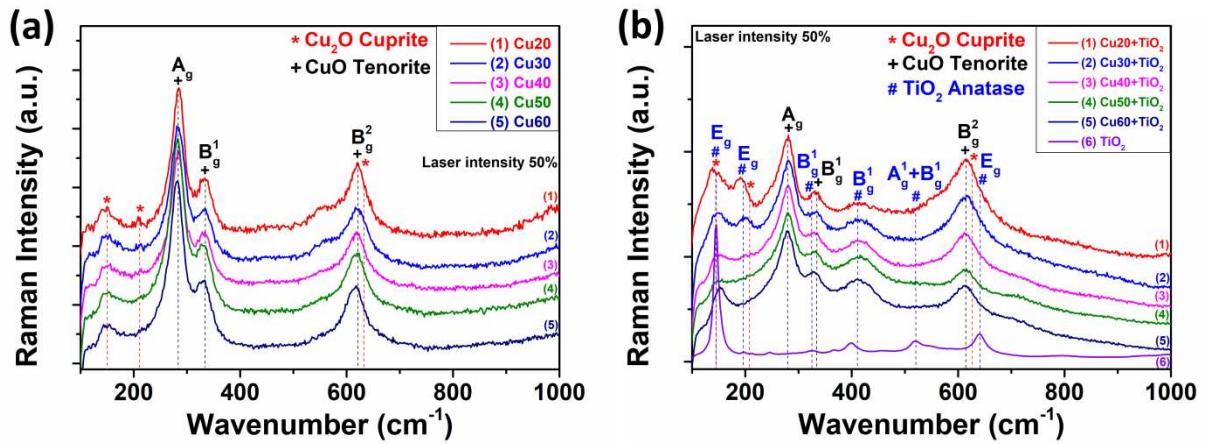
Figure S2. Micro-Raman spectra of thin nanocrystalline films of (a) CuO/Cu$_2$O and (b) TiO$_2$/CuO/Cu$_2$O. All samples were thermally annealed under air conditions at 420°C for 30 min for samples with thicknesses of 20 nm (Cu20), 30 nm (Cu30) and 40 nm (Cu40) and for 60 min for samples with thicknesses of 50 nm (Cu50) and 60 nm (Cu60).
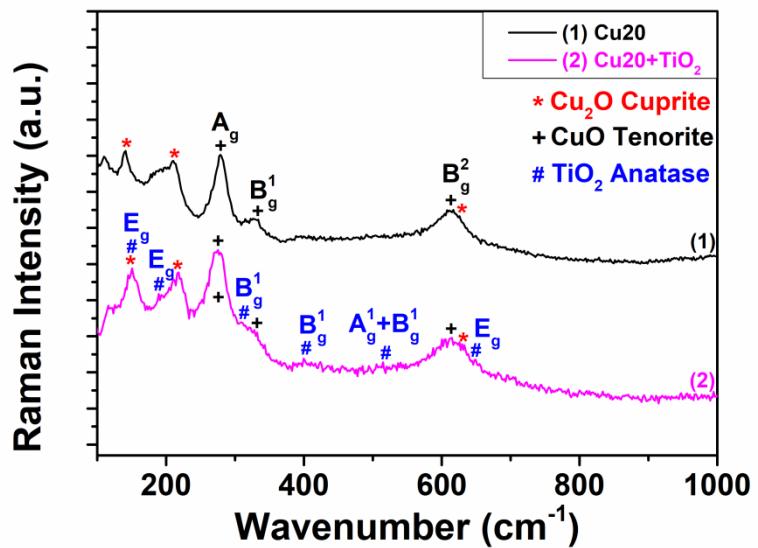
Figure S3. Micro-Raman spectra of CuO/Cu$_2$O and TiO$_2$/CuO/Cu$_2$O with 20 nm thickness thermally treated under air conditions at 420°C for 30 min.

Cuprite or cuprous oxide (Cu_2O) has a simple cubic unit cell given its translational symmetry. This material which has cubic symmetry at the centre of the zone, where exists direct exciton transitions, has isomorphous point groups k and O_h. The cuprite cubic structure can be described as two sub-lattices, a face-center cubic (fcc) one of copper cations and a body-center cubic (bcc) one of oxygen anions. The cuprite structure also has dichotomy [36,37], characterized by O atoms located in tetrahedral interstitial positions relative to the copper sublattice, allowing a tetrahedral coordination environment for the O ions, whereas Cu is linearly coordinated by two neighbouring oxygen anions. Note that these low coordination numbers are unconventional for metal oxides [37]. The short copper-oxygen bond length in Cu_2O is also unusual [37], as it is not compatible with the sum of the ionic radii for Cu^+ and O^{2-} reported in the literature [38]. The symmetries of the phonons and bands are readily collect by the method of Moskalenko [39]. The space group is $Pn\bar{3}m$ or O_h^4 (point symmetry O_h, or $m3m$) for the Cu_2O crystal with a simple cubic Bravais lattice [36,40,41], containing two formula units in the unit cell, which explains that optical phonons exist at 15 zone centres. The symmetry of the zone centre normal modes are given by [42–44]:

$$\Gamma_{Cu_2O} = A_{2u} + E_u + 3T_{1u} + T_{2u} + T_{2g} \tag{S2}$$

CuO crystallizes in the monoclinic crystal system (space group symmetry $C_{2h}^6 \left[C2/c \right]$) [42–45]. Thus, this material has 12 vibrational modes, which are optically active phonon modes, at the zone centre. The two copper atoms in the primitive cell are on sites with the $C_1(2)$ symmetry and the oxygen atoms are on sites with the $C_2(2)$ symmetry [42–45]. The site symmetries as well as the factor group allow the following zone centre normal modes [42–45]:

$$\Gamma = 4A_u + 5B_u + A_g + 2B_g \tag{S3}$$

The three $A_g + 2B_g$ modes are Raman active and the three acoustic modes are represented by $A_u + 2B_u$, whereas the remaining six modes are infrared active [42–46]. The lattice dynamics of Cu_2O and CuO have been previously investigated in different works [46–49].

The micro-Raman spectra investigated at room temperature for the CuO/Cu_2O and TiO_2/CuO/Cu_2O nano-materials in the range 100-1000 cm^{-1} is shown in **Figure S2**. The presence of Cu metal, could not be ascertained from these measurements due to instrumental limitations and because materials possessing negative real and imaginary positive dielectric constants, such as metals, exhibit surface plasmon resonance (SPR) [50,51]. The micro-Raman spectrum investigated at room-temperature for the six samples contain three main peaks at ~144, 212 and 628 cm^{-1}, which are attributed to the Cu_2O crystalline phase. Co-existence of the Cu_2O and CuO phases for specimens thermally annealed at 420°C for 1 h was confirmed by the data presented in **Figure S2a** and **S2b**, which displays strong peaks at 298, 345, and 632 cm^{-1} [52]. Based on the high sensitivity of the micro-Raman spectroscopy for the investigations of the surface regions of the samples [53], the stronger peaks attributed to the CuO phase (curve (2) in **Figure S3**) indicate the formation of CuO above the surface of the Cu_2O nano-crystals substrate. At temperatures higher than 420°C for thermally annealed samples, the peaks ascribed to the Cu_2O crystalline phase vanish in the micro-Raman spectra (not shown), which can be attributed to the formation of a thicker layer of CuO on top of Cu_2O [53]. The micro-Raman spectra of the TiO_2 films covering the ultra-thin CuO/Cu_2O layers with different thicknesses (20, 30, 40, 50, and 60 nm) thermally annealed at 420°C for 0.5 or 1 h are reported in **Figure S2b**. In the case of the TiO_2/CuO/Cu_2O samples, the results demonstrate the same trend and are not discussed here to avoid repetition. The MR results obtained are in good agreement with our XPS data, confirming that the Cu_2O phase transform into the CuO crystalline phase after the thermal annealing treatment.

The anatase phase has the $D_{4h}^{19}(I4/amd)$ space group [54,55] formula units in the primitive unit cell (see **Figure S3**). The modes at the Γ point belong to the following representation [54,55]:

$$\Gamma_{opt} = 1A_{1g} + 1A_{2u} + 2B_{1g} + 1B_{2u} + 3E_g + 2E_u \qquad (S4)$$

The A_{1g}, B_{1g} and E_g modes are Raman active, whereas the A_{2u} and the two E_u modes are infrared active. The peaks at about ~144, ~197, ~326, ~400, ~13–517, and ~635 cm^{-1} from **Figure S2b**

(curve 7) can be attributed to the E_g, E_g, B_{1g}, B_{1g}, A_{1g}+ B_{1g}, and E_g modes of anatase, respectively [54–57], which correlate well with the anatase phase in the TiO_2 film [58].
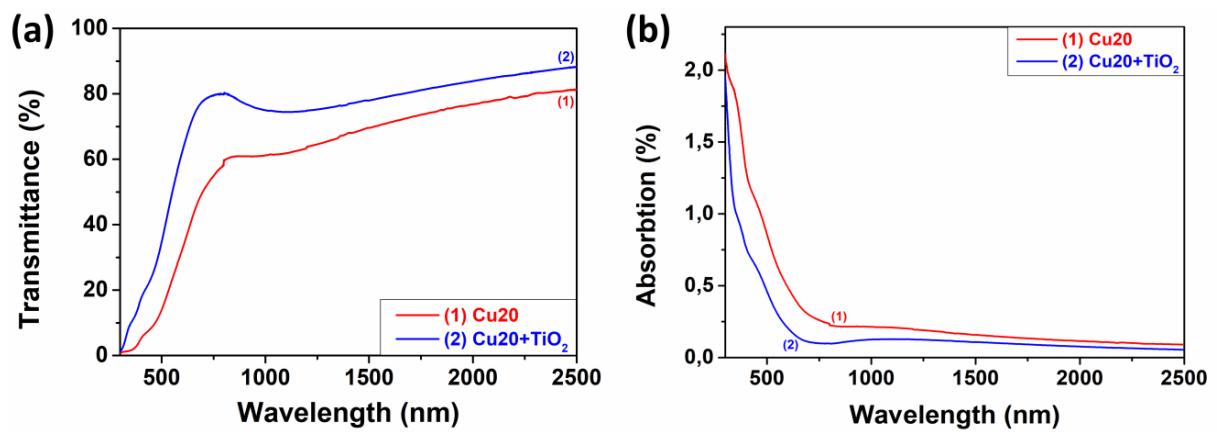
Figure S4. (a) Transmission spectra and (b) plot of absorption near the UV edge *vs*. wavelength of the TiO$_2$/CuO/Cu$_2$O heterostructure with a thickness of 20 nm thermally treated at 420°C for 0.5 h.
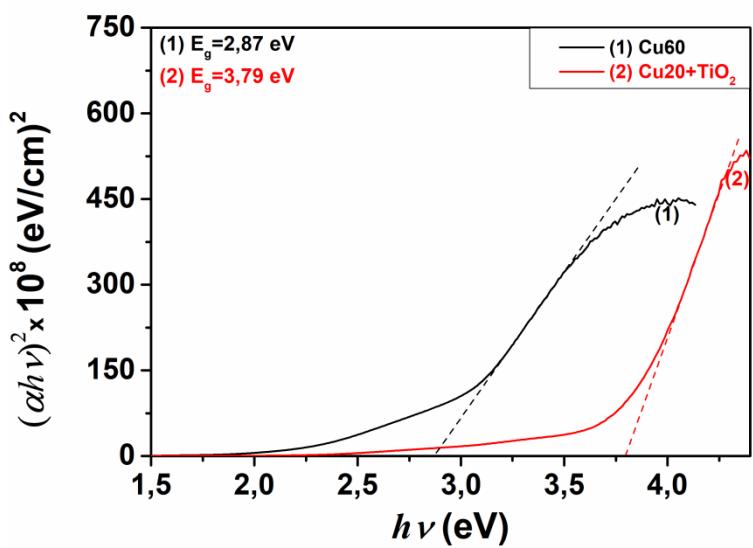
Figure S5. Plot of $(\alpha h\nu)^2$ *vs*. photon energy $h\nu$ for the CuO/Cu$_2$O and TiO$_2$/CuO/Cu$_2$O heterostructures, with a thickness of 60 nm (Cu60) and 20 nm (Cu20), respectively.
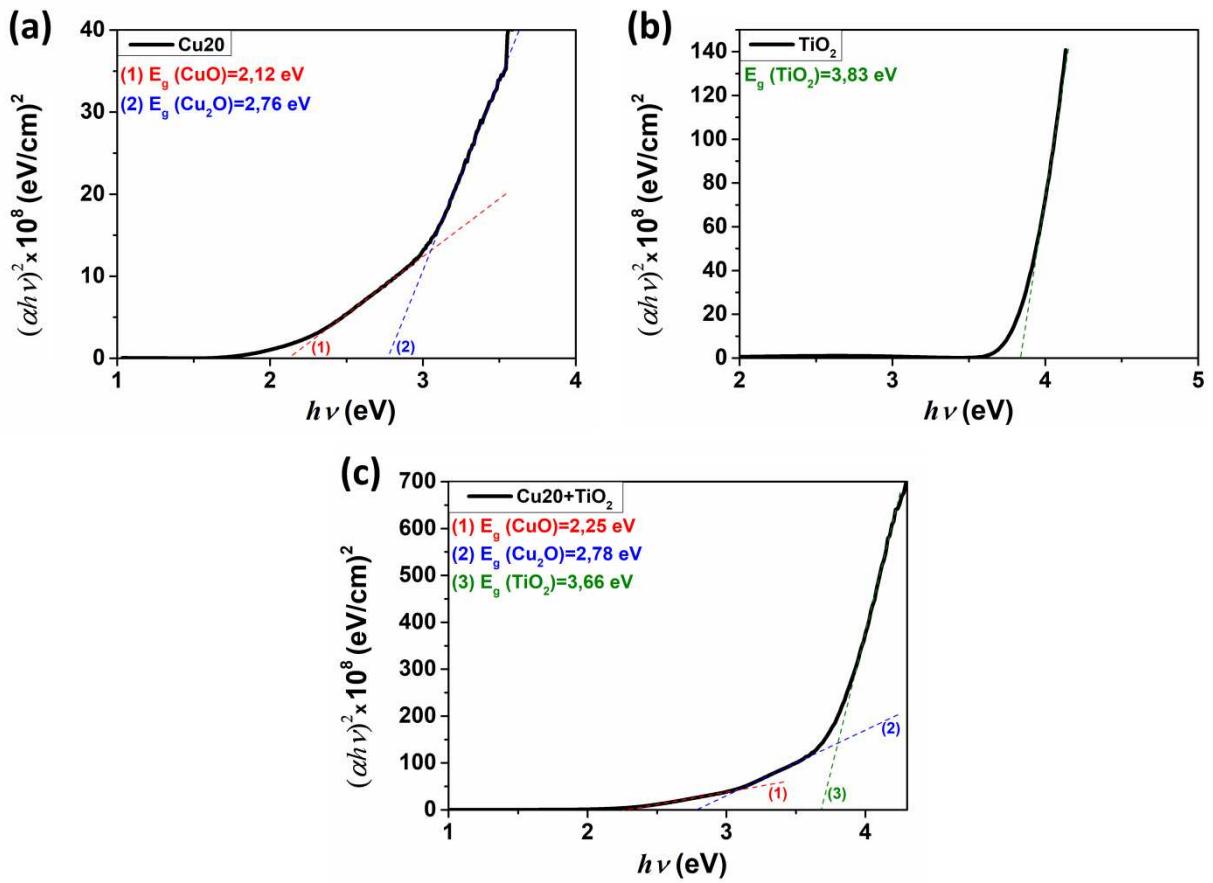
Figure S6. Plot of $(\alpha h\nu)^2$ vs. $h\nu$ for: a) CuO/Cu$_2$O; b) TiO$_2$; and c) TiO$_2$/CuO/Cu$_2$O.

Supporting Information Text S3

The absorption versus wavelength spectra shows only one absorption peak centered at around 400 - 500 nm (**Figure S4b**). The optical characteristics of the prepared heterostructure and the estimation of its optical bandgap energy mean value are extremely important for the development of sensor applications. According to the Tauc method, the optical band gap of the CuO nanomaterial follows the equations [59,60]:

$$\alpha h v = k\sqrt{h v - E_g} \; ; \qquad \alpha E_p = k(E_p - E_g)^n \tag{S5}$$

where, α is the optical absorption edge, which is proportional to the absorbance (the absorption coefficient of the material), $E_p = h v$ –is the energy of the incident photon, k is a proportionality constant dependent on the material structure, E_g is the optical band gap, and h is the Planck constant. Since the value of the exponent n depends on the nature of the optical transition , it can take the values 1/2, 3/2, 2 or 3 for direct allowed, direct forbidden, indirect allowed or indirect forbidden transitions, respectively [61,62]. The value of ½ is therefore used for CuO as both semiconducting oxides CuO and Cu_2O are direct-band-gap semiconductors [62], while E_g can be obtained from Eq. (S5). The absorption ($\alpha \geq 10^4$ cm^{-1}) is related to direct band transitions [63,64]. The optical bandgap E_g was found by extrapolating the linear portion (straight line) tangent of the $(\alpha h v)^2$ vs. $h v$ graph that intercepts the photon energy axis (i.e., $h v$, the abscissa) at $\alpha h v = 0$, as shown in **Figure S5**. We found that the bandgap energy is 2.3 eV for the as-grown CuO nanomaterials, which is larger than the value published for the CuO bulk material ($E_g = 1.855$eV) [65]. The optical band gap increases for the CuO nanolayers when we decrease their thickness and particle size, which can be assigned to quantum confinement effects [66].

Experimental data show only direct transition-related absorption peaks without indication of indirect transition absorption (**Figure S4b**). The large band gap detected could be associated to the existence of intra-gap states and quantum confinement effect [67]. It is known that the E_g of Cu_2O bulk material ranges from 2.0 to 2.5 eV. Thus, we believe that the difference of E_g between of the

Cu$_2$O ultra-thin films investigated in this study and in the values reported the literature is mainly caused by the quantum size effect in our samples.

Figure S4a shows the transmission spectra of the *CuO/Cu$_2$O* and *TiO$_2$/CuO/Cu$_2$O* heterostructures with a thicknesses of 20 nm treated at 420°C for 0.5 h. We can see that all samples possess good transmission over 70% beyond a wavelength of 600 nm. We also found that the *TiO$_2$/CuO/Cu$_2$O* sample (curve 2) have a higher transmittance than *CuO/Cu$_2$O* since the main mechanism of light trapping in the small absorbent TiO$_2$ films involves the scattering of light [68]. Figure S4b presents a plot of the absorption near the UV edge vs. wavelength for the same heterostructures shown in Figure S4a, clearly indicating two regions for the optical band gaps of each crystalline phase.

As calculated from the results in Figure S6a, the E_g of the CuO thin films is about 1.9 eV. The best linear fit was found when *n*=1/2, i.e. for a direct allowed optical transition in the copper oxide nanoparticles) [69,70]. The Tauc plots reported in Figure S6 confirm a rise in the bandgap from ~2.03 eV to ~2.87 eV with a decrease in the nanoparticle size from 30 nm to 10 nm. The absorption edge of ~2.03 eV for the 30 nm specimen is similar to the published value for bulk Cu$_2$O [69–72].

Table S1. Responses to ethanol of the CuO/Cu$_2$O and TiO$_2$/CuO/Cu$_2$O samples with thickness of

20 nm (Cu20) and 30 nm (Cu30) at the operating temperature of 350°C.

Heterostructure	Sample set	1 ppm			5 ppm			10 ppm		
		Gas response, (%)	Response time τ_r, (s)	Recovery time τ_d, (s)	Gas response, (%)	Response time τ_r, (s)	Recovery time τ_d, (s)	Gas response, (%)	Response time τ_r, (s)	Recovery time τ_d, (s)
CuO/Cu$_2$O	Cu20	~27	6.1	14.4	~36	13.4	13.2	~40	25.2	20.7
	Cu30	~31	5.4	14.3	~36	16.3	13.6	~45	9.6	18.8
TiO$_2$/CuO/Cu$_2$O	Cu20	~32	21.9	44.8	~39	17.2	40.6	~42	22.8	46.3
	Cu30	~30	21.4	30.1	~33	16.8	43.4	~42	23.2	30.3
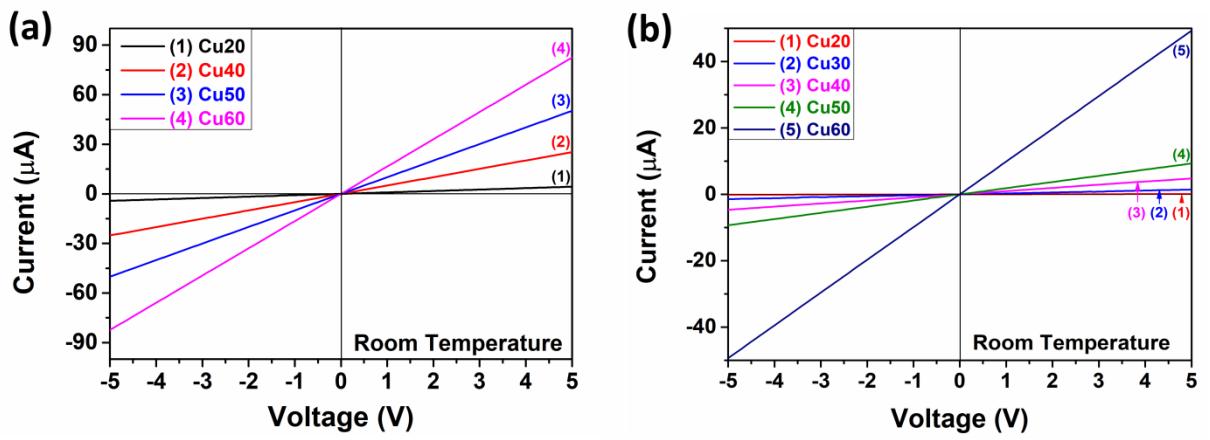
Figure S7. *I-V* current-voltage characteristics measured at room temperature for the: (a) CuO/Cu_2O and (b) $TiO_2/CuO/Cu_2O$ samples, with various thicknesses of 20 nm (Cu20), 30 nm (Cu30), 40 nm (Cu40), 50 nm (Cu50) and 60 nm (Cu60).
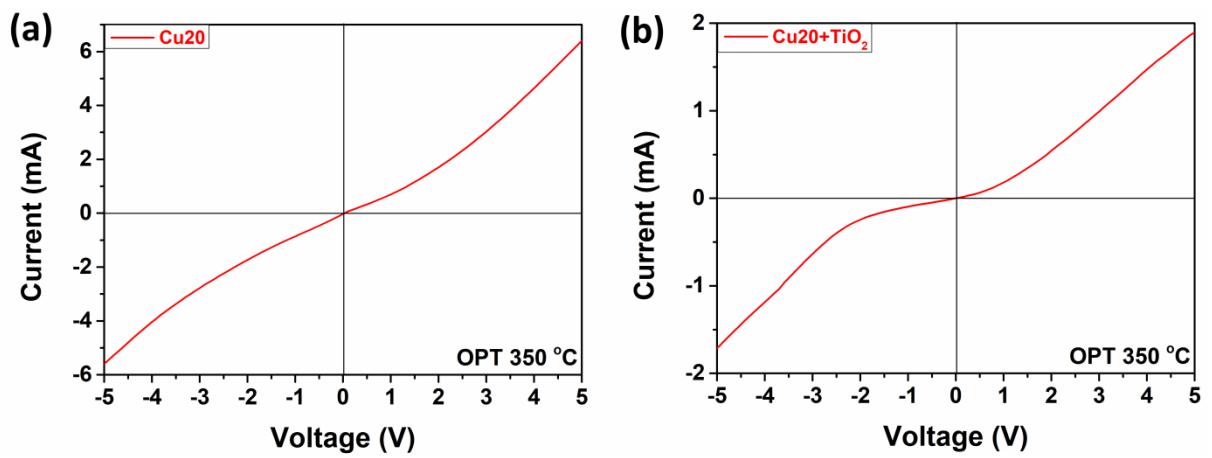
Figure S8. *I-V* current-voltage characteristics measured at the operating temperature of 350°C for the: (a) CuO/Cu$_2$O and (b) TiO$_2$/CuO/Cu$_2$O samples with a thickness of 20 nm (Cu20).
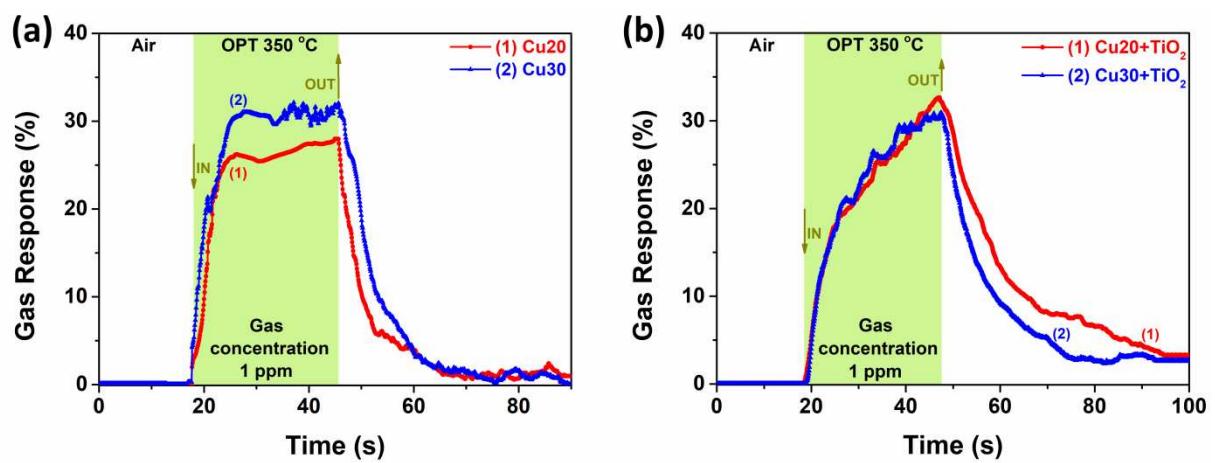
Figure S9. Dynamic response to 1 ppm concentration of ethanol vapor for: (a) CuO/Cu$_2$O; and

(b) TiO$_2$/CuO/Cu$_2$O samples with thicknesses of 20 nm (Cu20) and 30 nm (Cu30).
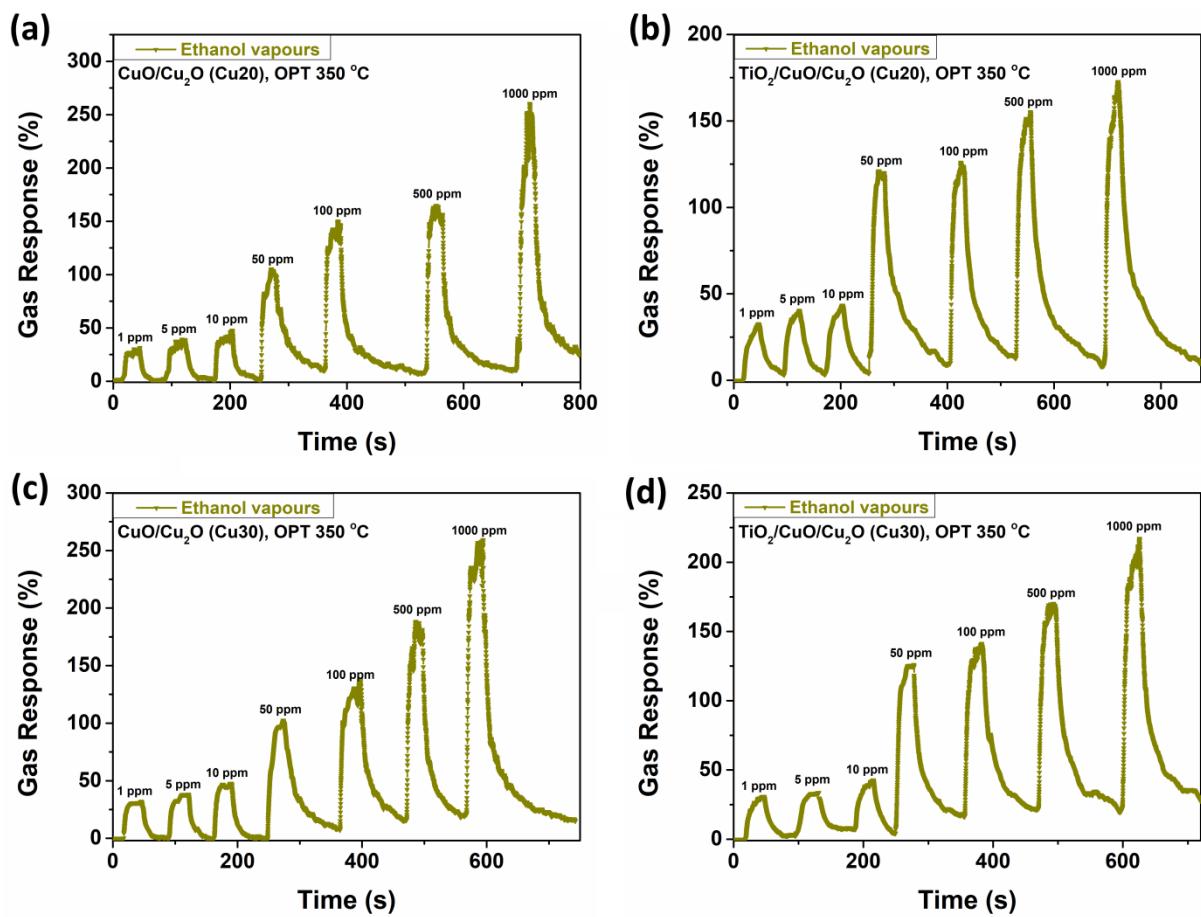
Figure S10. Dynamic response to different concentrations of ethanol for: (a) CuO/Cu$_2$O (Cu20) samples; (b) TiO$_2$/CuO/Cu$_2$O (Cu20) samples; (c) CuO/Cu$_2$O (Cu30) samples and (d) TiO$_2$/CuO/Cu$_2$O (Cu30) samples.
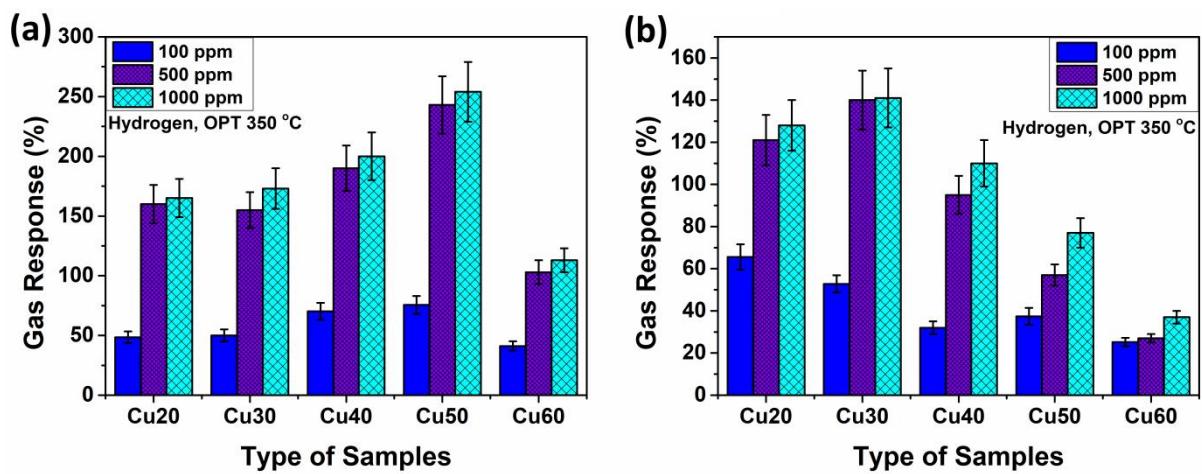
Figure S11. Gas response to different concentrations of hydrogen measured at 350°C versus the type of samples for: (a) CuO/Cu$_2$O and (b) TiO$_2$/CuO/Cu$_2$O samples with different thicknesses of 20 nm (Cu20), 30 nm (Cu30), 40 nm (Cu40), 50 nm (Cu50) and 60 nm (Cu60), respectively.

Supporting Information Text S4

The electrical and chemical properties of the heterostructures' surfaces are explained as follows [44,73–75], when exposed to oxygen in ambient air at relatively low temperatures, a hole accumulation layer/zone (HAL) is formed at their surface.

$$O_2(gas) + 2e^- \rightarrow 2O^-(ads). \tag{S6}$$

At temperatures slightly above 150°C, oxygen species become adsorbed on the copper oxide surface following the reaction [44,76]:

$$\frac{1}{2}O_2(gas) \xleftrightarrow{150^oC} O^-(ads) + h^+, \tag{S7}$$

where $O_{2(gas)}$ are the oxygen molecules in air, $O^-_{(ad)}$ are the oxygen ions adsorbed on the oxide surfaces, and h^+ are the holes released in oxide. Thus, due to the formation of HAL at the oxide surface, the electrical resistivity of the top layer becomes lower than at the subsurface layers, which is considered to be an insulating region according to previous works [77–82].

Based on previous results [83,84], oxygen ions adsorb on the semiconducting oxide surface in different forms, such as O_2^-, O^-, and O^{2-} (20°C–500°C), as demonstrated by TPD, ESR, and FTIR. Molecular O_2^- and atomic O^- species dominate below 150°C and between 150°C–500°C, respectively. At room temperature, the O_2^- molecules species trap electrons from the copper oxide. Therefore, the conductivity of the heterostructure decreases due to the increasing concentration of holes at the surfaces produced during the process of trapping electrons [55,83,84]. However, in the chemical detection at 300°C, O^- is frequently chemisorbed and the reaction kinetics are as follows. Once the sensor is exposed to ethanol vapors, a surface reaction takes place between the ethanol molecules and the adsorbed oxygen species on the copper oxide. As a result, ethanol C_2H_5OH molecules are oxidized to CO_2 and H_2O and the HAL region is reduced [44,77,79,81,82,85]:

$$C_2H_5OH + 6O^-_{(ads)} \rightarrow 2CO_{2(gas)} + 3H_2O_{(gas)} + 6e^-. \tag{S8}$$
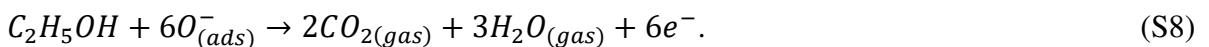
Thus, according to the reaction above, a single ethanol molecule interacts with six of the adsorbed oxygen ions where 6 electrons are released, which recombine with the holes in the HAL

region, therefore reducing its size. This leads to an increase in the electrical resistance and decreases the electrical current flow in this region [44,79,85]. Based on previous works, the width of HAL region lies between 5.2 to 16.5 nm for the ultrathin top CuO phase, which is completely affected by surface reactions. Due to the low upper valence band level of the Cu_2O core, holes flow from it to the surface-CuO layers, which affects the CuO/Cu_2O interface and contributes to the sensing mechanism. The HAL region (with a total width estimated around 20 nm) is the preferential path for the electrical conduction due to the lower resistance of CuO compared to the core Cu_2O. The small average diameter of the nanocrystals ensures a high surface-to-volume ratio, allowing more adsorbed oxygen species on the heterostructures' surface, which enhances the ethanol sensing and explains the better performances towards ethanol vapor detection. Our experimental data fully support these reaction mechanisms: when EtOH is introduced in the test chamber, the current decreases and the resistance increases. The CuO/Cu_2O heterostructures induce a large HAL region due to the ultra-thin top CuO layer and charge diffusion effects at the interface. Therefore, the change in the electrical resistance will be larger under exposure to ethanol vapor compared to the single phase material-sensor.

Concerning the ethanol detection mechanism for the $TiO_2/CuO/Cu_2O$ heterostructures, the presence of a *p-n* heterojunction between TiO_2 and CuO/Cu_2O leads to bending of the energy bands in the depletion region (**Figure S12**) and to an electrical field due to electron transfer in the *p-type* CuO/Cu_2O layer and holes in the *n-type* TiO_2 material, which appear until the system reaches the equilibrium of Fermi levels (**Figure S12b**). The electrical field at the interface will help/enhance the charge transfer efficiency to the adsorbed oxygen molecules at the semiconducting oxide surface.

Such a type of contact between two different semiconducting oxides forms a non-planar *p-n* heterojunction at the interface between CuO/Cu_2O and TiO_2, which is useful for tuning chemical sensing properties [86]. From these data, we can argue that the *p-type* CuO/Cu_2O layer withdraws

electrons from donor defects, such as oxygen vacancies from TiO_2, decreasing the density of charge carriers [87,88] and increasing the resistance of the heterostructure.

When CuO/Cu_2O, which possess *p-type* electrical conductivity [44,82], and TiO_2, *n-type* [55,89,90], are put in contact forming the heterostructures *p-type* conductivity is measured, demonstrating that CuO/Cu_2O predominates.

Adsorbed oxygen on surface of TiO_2 traps conduction electrons following different reactions depending in operating temperature [55,84,91–93]:

$$O_{2(gas)} \leftrightarrow O_{2(ads)} \tag{S9}$$

$$O_{2(ads)} + e^- \rightarrow O_{2(ads)}^- \tag{S10}$$

$$O_{2(ads)}^- + e^- \leftrightarrow 2O_{(ads)}^- \tag{S11}$$

$$O_{(ads)}^- + e^- \leftrightarrow O_{(ads)}^{2-}. \tag{S12}$$
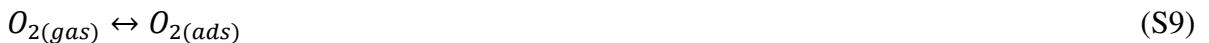
When the $TiO_2/CuO/Cu_2O$ heterostructures are exposed to ethanol vapors, a chemical reaction between C_2H_5OH and the adsorbed oxygen species takes place on the TiO_2 surface, where electrons are released in the conduction band of titania [94]. Possible reaction paths are listed below (Eq. (S13)) [95]:

$$C_2H_5OH + O^-(O^{2-}/O_2^-) \rightarrow \begin{cases} CH_3CHO + H_2O + e^- \\ CO_2 + H_2O + e^- \end{cases} \tag{S13}$$

$$C_2H_5OH + h^+ + O^-(O^{2-}/O_2^-) \rightarrow CH_3CHO + H_2O \tag{S14}$$

$$C_2H_5OH + h^+ + O^-(O^{2-}/O_2^-) \rightarrow CO_2 + H_2O \tag{S15}$$
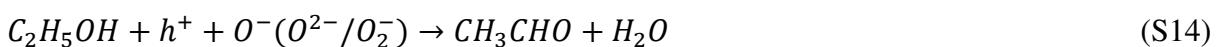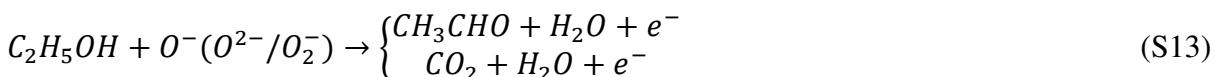
At the interface of the $TiO_2/CuO/Cu_2O$ heterostructures, the reduced ethanol molecule will be combined with the holes in CuO, producing the CH_3CHO intermediate that reacts with the oxygen adsorbed on the *n-type* TiO_2 overlayer (Eq. (S14) and (S15)). In general, *p-type* semiconducting oxides, such as CuO/Cu_2O, allow complete reaction of ethanol, which increases the sensing performances towards this molecule. This effect has been reported previously by other authors for CuO-SnO_2 [96], SnO_2 doped with Ni [97] co-doped ZnO [98], respectively.

When the $TiO_2/CuO/Cu_2O$ heterostructures are exposed to H_2 gas, the hydrogen molecules are oxidized, which releases electrons that narrow the electron depletion region as follows [99–101]:

$$\frac{1}{2} O_2^- + H_2 \rightarrow H_2O + e^- \tag{S16}$$

$$2O^- + 2H_2 \rightarrow 2H_2O + 2e^- \tag{S17}$$

This modifies the conduction channel width [87,88], which in our case increases the resistance of the sensor structure.
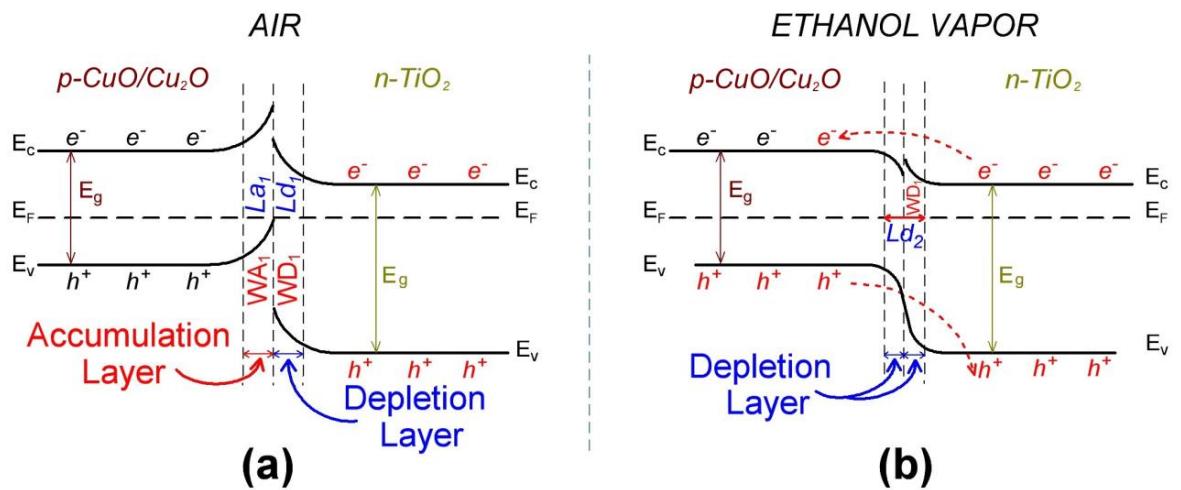
Figure S12. Energy band diagrams for the $TiO_2/CuO/Cu_2O$ heterostructures in: (a) air; and (b) under ethanol vapor.

Table S2. Calculated unit cell lattice parameters (*a*, *b* and *c*), atomic charges (*q*), atomic magnetic moments (*m*) and band gap energy (E_g) for the cubic cuprite Cu_2O, monoclinic tenorite CuO and tetragonal anatase TiO_2. Calculated staggering parameter *y* and angle *β* are reported for CuO. Oxidation state (OS) and experimental values for *a*, *b*, *c*, *y*, *β*, *m* and E_g are indicated for all phases.

		Cu_2O	CuO	TiO_2
a (Å)	Calc.	4.256	4.706	3.845
	Exp.	4.268 [102]	4.687 [103]	3.785 [104]
b (Å)	Calc.	--	3.438	--
	Exp.	--	3.424 [103]	--
c (Å)	Calc.	--	5.153	9.663
	Exp.	--	5.132 [103]	9.512 [104]
y	Calc.	--	0.422	--
	Exp.	--	0.418 [103]	--
β (°)	Calc.	--	99.5	--
	Exp.	--	99.5 [103]	--
$q_{Cu/Ti}$ (e⁻ atom⁻¹) $OS_{Cu/Ti}$	Calc.	+0.535 +1	+1.081 +2	+2.391 +4
q_O (e⁻ atom⁻¹) OS_O	Calc.	−1.070 −2	−1.081 −2	−1.196 −2
$m_{Cu/Ti}$ (μ_B atom⁻¹)	Calc.	0.000	0.682	0.000
	Exp.	0.000	0.60−0.68 [105–108]	0.000
m_O (μ_B atom⁻¹)	Calc.	0.000	0.319	0.000
	Exp.	0.000	--	0.000
E_g (eV)	Calc.	0.737	1.66	2.57
	Exp.	2.00−2.40 [109,110]	1.00−1.90 [105,106,109–112]	3.00−3.15 [113–116]

Supporting Information Text S5

Table S2 displays the calculated Bader charges [117–119], which are +0.535, +1.081 and +2.391 for

Cu in Cu_2O, Cu in CuO and Ti, respectively. Although the Bader charge is just above 50% of the

formal oxidation state for Cu^{1+}, we noted that their values are slightly larger for Cu^{2+} and even

bigger for the Ti^{4+} atoms. The underestimation of charges is a known effect of the Bader population

scheme [120–125], which is based upon the charge density, being independent of the atomic oxidation

states and basis set used, unlike wavefunction based partitioning methodologies [126–128]. We

observed the same trends for the Bader charges of the O anions than for their counter-cations,

given the equal number of electrons that are transferred between their neutral atoms during

formation of the bulk phases. Cu_2O and TiO_2 are predicted as non-magnetic since the $3d$ shells of

Cu^{1+} and Ti^{4+} are full and empty, respectively. The inferred magnetic moment is $m_{Cu} = 0.682\ \mu_B$

$atom^{-1}$ for CuO, in excellent agreement with previous calculations [105,106] and experiments [107,108].

The magnetic moment for Cu^{2+}, which is 32% below the value of 1 μ_B $atom^{-1}$ expected for an ion

with a single unpaired electron and the electronic distribution $[Ar]3d^9$, induces a small magnetic

moment of $m_O = 0.319\ \mu_B$ $atom^{-1}$ to the O counter-anions. However, the total magnetic moment is

$M_S = 1.000\ \mu_B$ $f.u.^{-1}$ suggesting that CuO has half-metallic properties [122,129–132]. The band gap

energy calculated for Cu_2O is underestimated by 1.3 eV with respect to the value obtained from

optical absorption experiments [109], and X-ray photoemission and Bremsstrahlung isochromat

spectroscopy [110]. However, we found a much closer agreement for TiO_2, with a difference of just

0.43 eV between the simulated band gap energy and the range of values reported [113–116]. We also

simulated an exceptionally good band gap energy of $E_g = 1.66$ eV for CuO compared to other

simulations [105,106] and experiments [109–112].
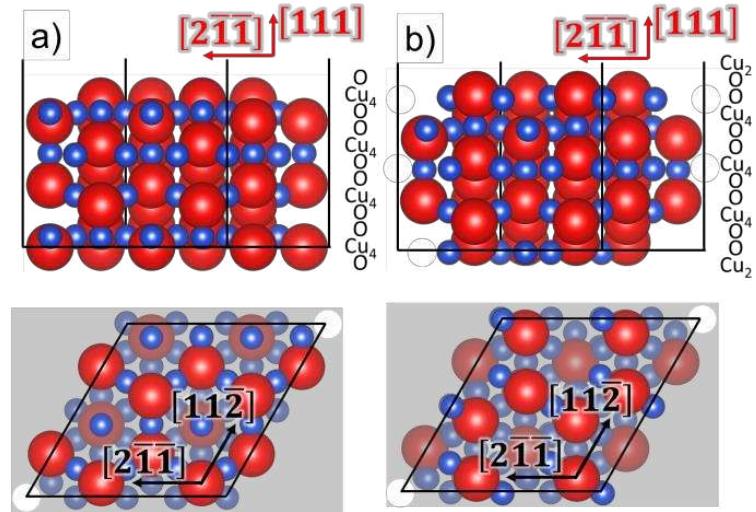
Figure S13. Side (top panels) and top (bottom panels) views of the optimised structures for terminations (a) *A* and (b) *B* of the $Cu_2O(111)$ surface. Crystallographic directions and stacking sequence of the atomic layers are indicated. Layers with atoms with dangling bonds are highlighted in the top view. O atoms are in red and Cu atoms are in dark blue.
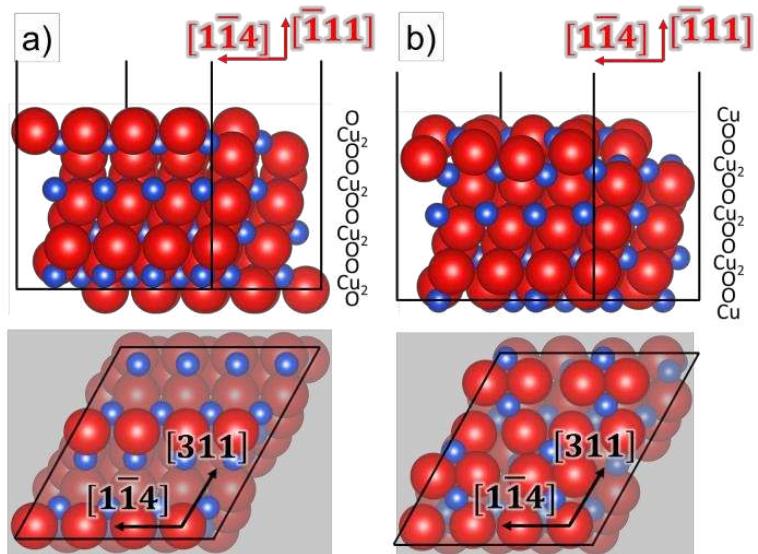
Figure S14. Side (top panels) and top (bottom panels) views of the optimised structures for terminations (a) *A* and (b) *B* of the CuO($\bar{1}11$) surface. Crystallographic directions and stacking sequence of the atomic layers are indicated. Layers with atoms with dangling bonds are highlighted in the top view. O atoms are in red and Cu atoms are in dark blue.
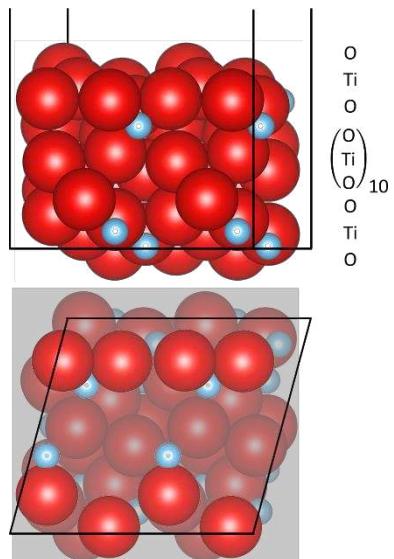
Figure S15. Side (top panel) and top (bottom panel) views of the optimised structures of the TiO$_2$(111) surface. Crystallographic directions and stacking sequence of the atomic layers are indicated. Layers with atoms with dangling bonds are highlighted in the top view. O atoms are in red and Ti atoms are in light blue.

Table S3. Surface energies before (γ_u) and after relaxation (γ_r) and the percentage of relaxation (R) for terminations A and B of the pristine $Cu_2O(111)$, $CuO(\bar{1}11)$ and $TiO_2(111)$ surfaces. The average atomic charges (q), average magnetic moments (m) and work function (Φ), are also indicated for each surface.

Surface	$Cu_2O(111)$		$CuO(\bar{1}11)$		$TiO_2(111)$
Termination	A	B	A	B	
γ_u (meV Å^{-2})	73	148	93	188	1156
γ_r (meV Å^{-2})	70	88	74	116	1044
R (%)	4.08	40.42	20.44	38.56	9.69
$q_{Cu/Ti}$ (e$^-$ atom^{-1})	+0.504	+0.512	+1.006	+1.017	+2.301
q_O (e$^-$ atom^{-1})	−1.007	−1.011	−1.017	−1.009	−1.134
$m_{Cu/Ti}$ (μ_B atom^{-1})	0.000	0.000	0.626	0.622	0.000
m_O (μ_B atom^{-1})	0.000	0.000	0.298	0.382	0.000
Φ (eV)	4.831	5.037	5.943	5.229	5.461

Table S4. Geometric misfit parameter (ζ) and interfacial free energy (σ_{int}) for CuO($\bar{1}$11) on Cu$_2$O(111) and TiO$_2$(111) on CuO($\bar{1}$11)/Cu$_2$O(111). The average atomic charges (q), average magnetic moments (m) and work function (Φ), are also indicated for each surface.

Heterojunction	CuO($\bar{1}$11)/Cu$_2$O(111)	TiO$_2$(111)/CuO($\bar{1}$11)/Cu$_2$O(111)
ζ (%)	1.66	6.97
σ_{int} (meV Å^{-2})	91	112
$q_{Cu/Ti}$ (e$^-$ atom^{-1})	+0.867	+2.325
q_O (e$^-$ atom^{-1})	−0.965	−1.130
$m_{Cu/Ti}$ (μ_B atom^{-1})	0.178	0.017
m_O (μ_B atom^{-1})	0.124	0.039
Φ (eV)	6.285	7.454

Table S5. Adsorption energies (E_{ads}) and charge transfers (Δq) for H_2, C_2H_5OH and n-C_4H_9OH on the heterostructures $CuO(\bar{1}11)/Cu_2O(111)$ and $TiO_2(111)/CuO(\bar{1}11)/Cu_2O(111)$. The adsorption site of the adsorbate on the surface of the heterostructures is also indicated. A negative value of Δq denote that the adsorbate loses electronic charge.

Adsorbate	$CuO(\bar{1}11)/Cu_2O(111)$			$TiO_2(111)/CuO(\bar{1}11)/Cu_2O(111)$		
	Site	E_{ads} (eV)	Δq (e⁻)	Site	E_{ads} (eV)	Δq (e⁻)
H_2	ridge 3-fold O	−0.117	−0.119	O	−0.182	0.003
	grove 3-fold O	−0.171	0.002		--	--
C_2H_5OH	3-fold Cu	−1.072	−0.095	Ti	−0.820	−0.089
	4-fold Cu	−0.793	−0.029		--	--
n-C_4H_9OH	3-fold Cu	−0.833	−0.062	Ti	−0.750	−0.070
	4-fold Cu	−0.788	−0.023		--	--
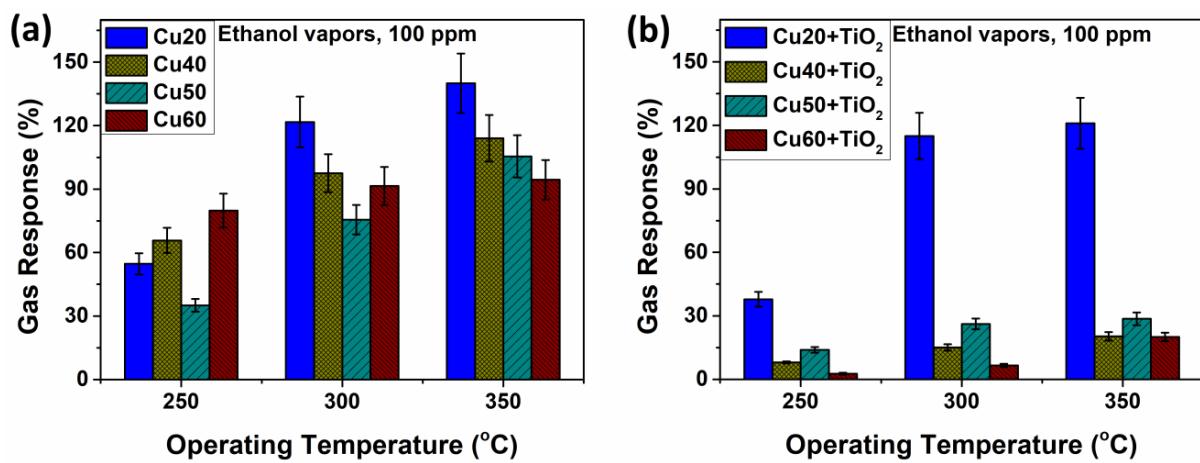
Figure S16. Response to 100 ppm of ethanol versus operating temperature for the: (a) CuO/Cu_2O; and (b) $TiO_2/CuO/Cu_2O$ samples with different thicknesses of 20 nm (Cu20), 40 nm (Cu40), 50 nm (Cu50) and 60 nm (Cu60).
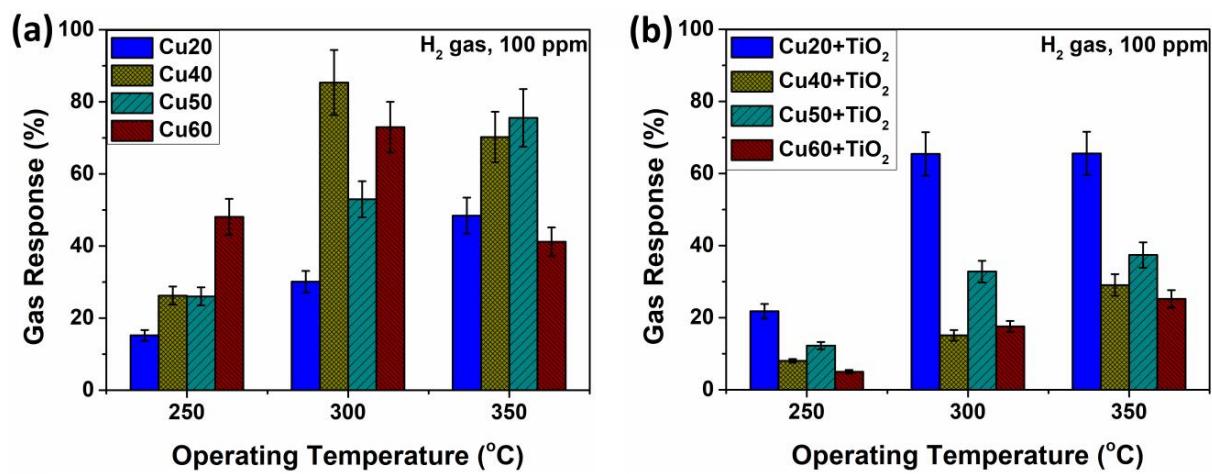
Figure S17. Response to 100 ppm of hydrogen versus operating temperature for the: (a) CuO/Cu$_2$O; and (b) TiO$_2$/CuO/Cu$_2$O samples with different thicknesses of 20 nm (Cu20), 40 nm (Cu40), 50 nm (Cu50) and 60 nm (Cu60).
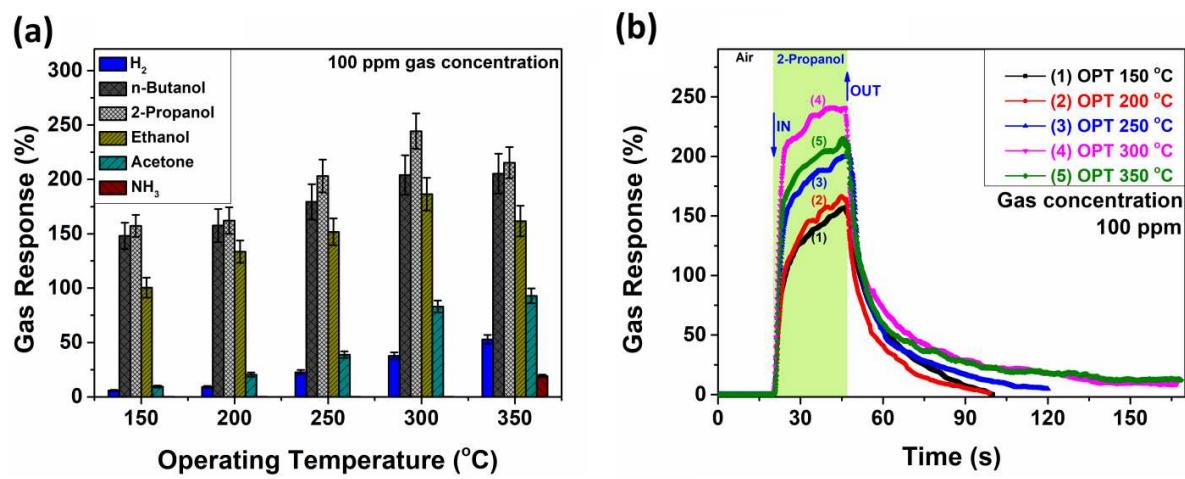
Figure S18. (a) Response to different gases (hydrogen, *n*-butanol, 2-propanol, ethanol, acetone and ammonia) versus operating temperature for the $TiO_2/CuO/Cu_2O$ sample set with a thickness of 30 nm (Cu30); (b) Dynamic response to 2-propanol of the $TiO_2/CuO/Cu_2O$ sample set with a thickness of 30 nm (Cu30) at different operating temperature.
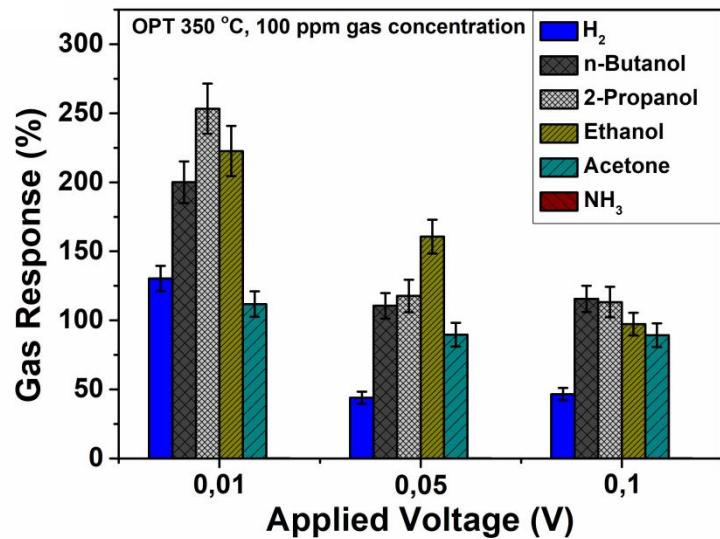
Figure S19. Response to different gases (hydrogen, *n*-butanol, 2-propanol, ethanol, acetone and ammonia) versus applied voltage for the $TiO_2/CuO/Cu_2O$ samples with a thickness of 20 nm (Cu20).
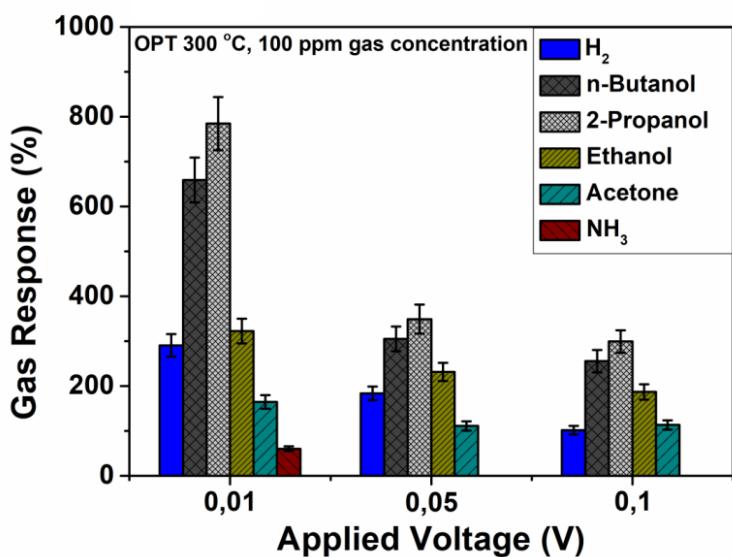
Figure S20. Response to different gases (hydrogen, *n*-butanol, 2-propanol, ethanol, acetone and ammonia) versus applied voltage for the $TiO_2/CuO/Cu_2O$ samples with a thickness of 30 nm (Cu30).
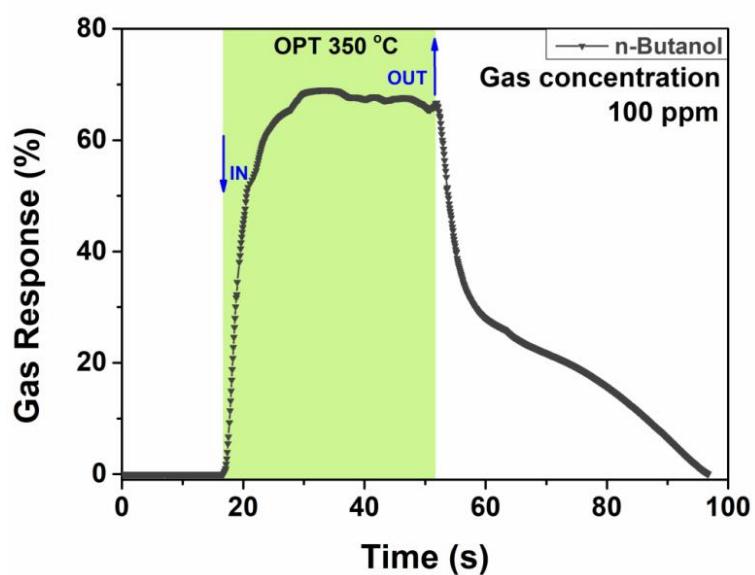
Figure S21. Dynamic response to *n*-butanol for the $TiO_2/CuO/Cu_2O$ sample set with a thickness

of   20 nm (Cu20).
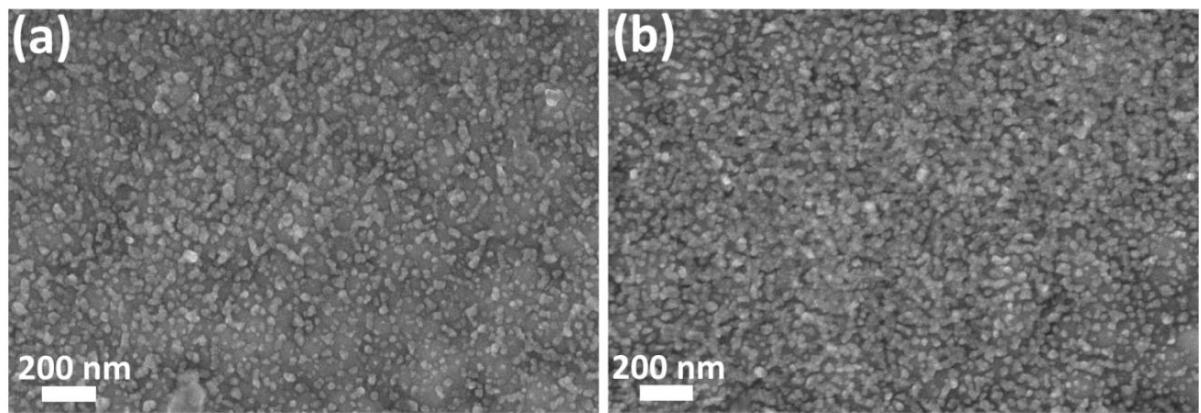
Figure S22. SEM images of the TiO$_2$/CuO/Cu$_2$O samples at lower magnification with different thickness of: (a) 20 nm and (b) 40 nm.

References

(1)   Kresse, G.; Hafner, J. Ab Initio Molecular Dynamics for Liquid Metals. *Phys. Rev. B* **1993**, *47* (1), 558–561.

(2)   Kresse, G.; Hafner, J. Ab Initio Molecular-Dynamics Simulation of the Liquid-Metal–Amorphous-Semiconductor Transition in Germanium. *Phys. Rev. B* **1994**, *49* (20), 14251–14269.

(3)   Kresse, G.; Furthmüller, J. Efficient Iterative Schemes for Ab Initio Total-Energy Calculations Using a Plane-Wave Basis Set. *Phys. Rev. B* **1996**, *54* (16), 11169–11186.

(4)   Kresse, G.; Furthmüller, J. Efficiency of Ab-Initio Total Energy Calculations for Metals and Semiconductors Using a Plane-Wave Basis Set. *Comput. Mater. Sci.* **1996**, *6* (1), 15–50.

(5)   Perdew, J. P.; Burke, K.; Ernzerhof, M. Generalized Gradient Approximation Made Simple [Phys. Rev. Lett. 77, 3865 (1996)]. *Phys. Rev. Lett.* **1997**, *78* (7), 1396–1396.

(6)   Blöchl, P. E. Projector Augmented-Wave Method. *Phys. Rev. B* **1994**, *50* (24), 17953–17979.

(7)   Kresse, G.; Joubert, D. From Ultrasoft Pseudopotentials to the Projector Augmented-Wave Method. *Phys. Rev. B* **1999**, *59* (3), 1758–1775.

(8)   Grimme, S.; Antony, J.; Ehrlich, S.; Krieg, H. A Consistent and Accurate Ab Initio Parametrization of Density Functional Dispersion Correction (DFT-D) for the 94 Elements H-Pu. *J. Chem. Phys.* **2010**, *132* (15), 154104.

(9)   Grimme, S.; Ehrlich, S.; Goerigk, L. Effect of the Damping Function in Dispersion Corrected Density Functional Theory. *J. Comput. Chem.* **2011**, *32* (7), 1456–1465.

(10)   Farkaš, B.; Santos-Carballal, D.; Cadi-Essadek, A.; de Leeuw, N. H. A DFT+U Study of the Oxidation of Cobalt Nanoparticles: Implications for Biomedical Applications. *Materialia* **2019**, *7*, 100381.

(11)   Ungerer, M. J.; Santos-Carballal, D.; Cadi-Essadek, A.; van Sittert, C. G. C. E.; de Leeuw, N. H. Interaction of H_2O with the Platinum Pt (001), (011), and (111) Surfaces: A Density Functional Theory Study with Long-Range Dispersion Corrections. *J. Phys. Chem. C* **2019**, *123* (45), 27465–27476.

(12)   Botha, L. M.; Santos-Carballal, D.; Terranova, U.; Quesne, M. G.; Ungerer, M. J.; van Sittert, C. G. C. E.; de Leeuw, N. H. Mixing Thermodynamics and Electronic Structure of the $Pt_{1-x}Ni_x$ ($0 \leq x \leq 1$) Bimetallic Alloy. *RSC Adv.* **2019**, *9* (30), 16948–16954.

(13)   Santos-Carballal, D.; Ngoepe, P. E.; de Leeuw, N. H. Ab Initio Investigation of the Thermodynamics of Cation Distribution and of the Electronic and Magnetic Structures in the $LiMn_2O_4$ Spinel. *Phys. Rev. B* **2018**, *97* (8), 085126.

(14)   Posada-Pérez, S.; Santos-Carballal, D.; Terranova, U.; Roldan, A.; Illas, F.; de Leeuw, N. H. CO_2 Interaction with Violarite ($FeNi_2S_4$) Surfaces: A Dispersion-Corrected DFT Study. *Phys. Chem. Chem. Phys.* **2018**, *20* (31), 20439–20446.

(15)   Postica, V.; Vahl, A.; Strobel, J.; Santos-Carballal, D.; Lupan, O.; Cadi-Essadek, A.; De Leeuw, N. H.; Schütt, F.; Polonskyi, O.; Strunskus, T.; Baum, M.; Kienle, L.; Adelung, R.; Faupel, F. Tuning Doping and Surface Functionalization of Columnar Oxide Films for

Volatile Organic Compounds Sensing: Experiments and Theory. *J. Mater. Chem. A* **2018**, *6* (46), 23669–23682.

(16) Postica, V.; Vahl, A.; Santos-Carballal, D.; Dankwort, T.; Kienle, L.; Hoppe, M.; Cadi-Essadek, A.; de Leeuw, N. H.; Terasa, M.-I.; Adelung, R.; Faupel, F.; Lupan, O. Tuning ZnO Sensors Reactivity toward Volatile Organic Compounds via Ag Doping and Nanoparticle Functionalization. *ACS Appl. Mater. Interfaces* **2019**, *11* (34), 31452–31466.

(17) Reguera, L.; López, N. L.; Rodríguez-Hernández, J.; González, M.; Hernandez-Tamargo, C. E.; Santos-Carballal, D.; de Leeuw, N. H.; Reguera, E. Synthesis, Crystal Structures, and Properties of Zeolite-Like $T_3(H_3O)_2M(CN)_6]_2 \cdot uH_2O$ (T = Co, Zn; M = Ru, Os). *Eur. J. Inorg. Chem.* **2017**, *2017* (23), 2980–2989.

(18) Ramogayana, B.; Santos-Carballal, D.; Aparicio, P. A.; Quesne, M. G.; Maenetja, K. P.; Ngoepe, P. E.; de Leeuw, N. H. Ethylene Carbonate Adsorption on the Major Surfaces of Lithium Manganese Oxide $Li_{1-x}Mn_2O_4$ Spinel (0.000 < x < 0.375): A DFT+ U -D3 Study. *Phys. Chem. Chem. Phys.* **2020**, *22* (12), 6763–6771.

(19) Sheppard, D.; Terrell, R.; Henkelman, G. Optimization Methods for Finding Minimum Energy Paths. *J. Chem. Phys.* **2008**, *128* (13), 134106.

(20) Hestenes, M. R.; Stiefel, E. Methods of Conjugate Gradients for Solving Linear Systems. *Journal of Research of the National Bureau of Standards*. **1952**, p 409.

(21) Dudarev, S. L.; Botton, G. A.; Savrasov, S. Y.; Humphreys, C. J.; Sutton, A. P. Electron-Energy-Loss Spectra and the Structural Stability of Nickel Oxide: An LSDA+U Study. *Phys. Rev. B* **1998**, *57* (3), 1505–1509.

(22) Anisimov, V. I.; Korotin, M. A.; Zaanen, J.; Andersen, O. K. Spin Bags, Polarons, and Impurity Potentials in $La_{2-x}Sr_xCuO_4$ from First Principles. *Phys. Rev. Lett.* **1992**, *68* (3), 345–348.

(23) Setyawan, W.; Curtarolo, S. High-Throughput Electronic Band Structure Calculations: Challenges and Tools. *Comput. Mater. Sci.* **2010**, *49* (2), 299–312.

(24) Taylor, R. H.; Rose, F.; Toher, C.; Levy, O.; Yang, K.; Buongiorno Nardelli, M.; Curtarolo, S. A RESTful API for Exchanging Materials Data in the AFLOWLIB.Org Consortium. *Comput. Mater. Sci.* **2014**, *93*, 178–192.

(25) Calderon, C. E.; Plata, J. J.; Toher, C.; Oses, C.; Levy, O.; Fornari, M.; Natan, A.; Mehl, M. J.; Hart, G.; Buongiorno Nardelli, M.; Curtarolo, S. The AFLOW Standard for High-Throughput Materials Science Calculations. *Comput. Mater. Sci.* **2015**, *108*, 233–238.

(26) Setyawan, W.; Gaume, R. M.; Lam, S.; Feigelson, R. S.; Curtarolo, S. High-Throughput Combinatorial Database of Electronic Band Structures for Inorganic Scintillator Materials. *ACS Comb. Sci.* **2011**, *13* (4), 382–390.

(27) Wang, S.; Wang, Z.; Setyawan, W.; Mingo, N.; Curtarolo, S. Assessing the Thermoelectric Properties of Sintered Compounds via High-Throughput Ab-Initio Calculations. *Phys. Rev. X* **2011**, *1* (2), 1–8.

(28) Monkhorst, H. J.; Pack, J. D. Special Points for Brillouin-Zone Integrations. *Phys. Rev. B* **1976**, *13* (12), 5188–5192.

(29) Nolan, M.; Elliott, S. D. The P-Type Conduction Mechanism in Cu_2O: A First Principles Study. *Phys. Chem. Chem. Phys.* **2006**, *8* (45), 5350–5358.

(30) Ekuma, C. E.; Anisimov, V. I.; Moreno, J.; Jarrell, M. Electronic Structure and Spectra of CuO. *Eur. Phys. J. B* **2014**, *87* (1), 1–6.

(31) Scanlon, D. O.; Morgan, B. J.; Watson, G. W. Modeling the Polaronic Nature of P-Type Defects in Cu_2O: The Failure of GGA and GGA+U. *J. Chem. Phys.* **2009**, *131* (12), 124703.

(32) Sanjinés, R.; Tang, H.; Berger, H.; Gozzo, F.; Margaritondo, G.; Lévy, F. Electronic Structure of Anatase TiO_2 Oxide. *J. Appl. Phys.* **1994**, *75* (6), 2945–2951.

(33) Landmann, M.; Rauls, E.; Schmidt, W. G. The Electronic Structure and Optical Response of Rutile, Anatase and Brookite TiO_2. *J. Phys. Condens. Matter* **2012**, *24* (19), 195503.

(34) Mermin, N. D. Thermal Properties of the Inhomogeneous Electron Gas. *Phys. Rev.* **1965**, *137* (5A), A1441–A1443.

(35) Blöchl, P. E.; Jepsen, O.; Andersen, O. K. Improved Tetrahedron Method for Brillouin-Zone Integrations. *Phys. Rev. B* **1994**, *49* (23), 16223–16233.

(36) Meyer, B. K.; Polity, A.; Reppin, D.; Becker, M.; Hering, P.; Klar, P. J.; Sander, T.; Reindl, C.; Benz, J.; Eickhoff, M.; Heiliger, C.; Heinemann, M.; Bläsing, J.; Krost, A.; Shokovets, S.; Müller, C.; Ronning, C. Binary Copper Oxide Semiconductors: From Materials towards Devices. *Phys. status solidi* **2012**, *249* (8), 1487–1509.

(37) Korzhavyi, P. A.; Johansson, B. *Literature Review on the Properties of Cuprous Oxide Cu_2O and the Process of Copper Oxidation*; Sweden, **2011**.

(38) Wells, A. F. *Structural Inorganic Chemistry*, 5th ed.; Oxford [Oxfordshire] Clarendon Press, **1984**.

(39) Moskalenko, S. Exciton Absorption of Light in a Cu_2O Crystal 1. Absence of Constant External Fields. *Sov. Phys. Solid State* **1961**, *2*, 1587–1596.

(40) Heinemann, M.; Eifert, B.; Heiliger, C. Band Structure and Phase Stability of the Copper Oxides Cu_2O, CuO, and Cu_4O_3. *Phys. Rev. B* **2013**, *87* (11), 115111.

(41) Reimann, K.; Syassen, K. Raman Scattering and Photoluminescence in Cu_2O under Hydrostatic Pressure. *Phys. Rev. B* **1989**, *39* (15), 11113–11119.

(42) Chrzanowski, J.; Irwin, J. C. Raman Scattering from Cupric Oxide. *Solid State Commun.* **1989**, *70* (1), 11–14.

(43) Åsbrink, S.; Norrby, L. J. A Refinement of the Crystal Structure of Copper(II) Oxide with a Discussion of Some Exceptional e.s.d.'s. *Acta Crystallogr. Sect. B Struct. Crystallogr. Cryst. Chem.* **1970**, *26* (1), 8–15.

(44) Lupan, O.; Cretu, V.; Postica, V.; Ababii, N.; Polonskyi, O.; Kaidas, V.; Schütt, F.; Mishra, Y. K.; Monaico, E.; Tiginyanu, I.; Sontea, V.; Strunskus, T.; Faupel, F.; Adelung, R. Enhanced Ethanol Vapour Sensing Performances of Copper Oxide Nanocrystals with Mixed Phases. *Sensors Actuators B Chem.* **2016**, *224*, 434–448.

(45) Zhang, Q.; Zhang, K.; Xu, D.; Yang, G.; Huang, H.; Nie, F.; Liu, C.; Yang, S. CuO Nanostructures: Synthesis, Characterization, Growth Mechanisms, Fundamental Properties, and Applications. *Prog. Mater. Sci.* **2014**, *60*, 208–337.

(46) Yu, T.; Zhao, X.; Shen, Z. .; Wu, Y. .; Su, W. . Investigation of Individual CuO Nanorods

by Polarized Micro-Raman Scattering. *J. Cryst. Growth* **2004**, *268* (3–4), 590–595.

(47)   Chou, M. H.; Liu, S. B.; Huang, C. Y.; Wu, S. Y.; Cheng, C.-L. Confocal Raman Spectroscopic Mapping Studies on a Single CuO Nanowire. *Appl. Surf. Sci.* **2008**, *254* (23), 7539–7543.

(48)   Bohnen, K.-P.; Heid, R.; Pintschovius, L.; Soon, A.; Stampfl, C. Ab Initio Lattice Dynamics and Thermal Expansion of Cu_2O. *Phys. Rev. B* **2009**, *80* (13), 134304.

(49)   Compaan, A.; Cummins, H. Z. Raman Scattering, Luminescence, and Exciton-Phonon Coupling in Cu_2O. *Phys. Rev. B* **1972**, *6* (12), 4753–4757.

(50)   Sahai, A.; Goswami, N.; Kaushik, S. D.; Tripathi, S. $Cu/Cu_2O/CuO$ Nanoparticles: Novel Synthesis by Exploding Wire Technique and Extensive Characterization. *Appl. Surf. Sci.* **2016**, *390*, 974–983.

(51)   Willets, K. A.; Van Duyne, R. P. Localized Surface Plasmon Resonance Spectroscopy and Sensing. *Annu. Rev. Phys. Chem.* **2007**, *58* (1), 267–297.

(52)   Hagemann, H.; Bill, H.; Sadowski, W.; Walker, E.; François, M. Raman Spectra of Single Crystal CuO. *Solid State Commun.* **1990**, *73* (6), 447–451.

(53)   Wagner, C. D.; Muilenberg, G. E. *Handbook of X-Ray Photoelectron Spectroscopy : A Reference Book of Standard Data for Use in x-Ray Photoelectron Spectroscopy*; Physical Electronics Division, Perkin-Elmer Corp.: Eden Prairie, Minn., **1979**.

(54)   Ohsaka, T.; Izumi, F.; Fujiki, Y. Raman Spectrum of Anatase, TiO_2. *J. Raman Spectrosc.* **1978**, *7* (6), 321–324.

(55)   Ababii, N.; Hoppe, M.; Shree, S.; Vahl, A.; Ulfa, M.; Pauporté, T.; Viana, B.; Cretu, V.; Magariu, N.; Postica, V.; Sontea, V.; Terasa, M.-I.; Polonskyi, O.; Faupel, F.; Adelung, R.; Lupan, O. Effect of Noble Metal Functionalization and Film Thickness on Sensing Properties of Sprayed TiO_2 Ultra-Thin Films. *Sensors Actuators A Phys.* **2019**, *293*, 242–258.

(56)   Enachi, M.; Lupan, O.; Braniste, T.; Sarua, A.; Chow, L.; Mishra, Y. K.; Gedamu, D.; Adelung, R.; Tiginyanu, I. Integration of Individual TiO_2 Nanotube on the Chip: Nanodevice for Hydrogen Sensing. *Phys. status solidi - Rapid Res. Lett.* **2015**, *9* (3), 171–174.

(57)   Lubas, M.; Jasinski, J. J.; Sitarz, M.; Kurpaska, L.; Podsiad, P.; Jasinski, J. Raman Spectroscopy of TiO_2 Thin Films Formed by Hybrid Treatment for Biomedical Applications. *Spectrochim. Acta Part A Mol. Biomol. Spectrosc.* **2014**, *133*, 867–871.

(58)   Nakaruk, A.; Ragazzon, D.; Sorrell, C. C. Anatase–Rutile Transformation through High-Temperature Annealing of Titania Films Produced by Ultrasonic Spray Pyrolysis. *Thin Solid Films* **2010**, *518* (14), 3735–3742.

(59)   Tsunekawa, S.; Fukuda, T.; Kasuya, A. Blue Shift in Ultraviolet Absorption Spectra of Monodisperse CeO_{2-x} Nanoparticles. *J. Appl. Phys.* **2000**, *87* (3), 1318–1321.

(60)   Moss, T. S. *Optical Properties of Semiconductors*; Butterworth: London, **1959**.

(61)   Erdoğan, İ. Y.; Güllü, Ö. Silicon MIS Diodes with Cr_2O_3 Nanofilm: Optical, Morphological/Structural and Electronic Transport Properties. *Appl. Surf. Sci.* **2010**, *256* (13), 4185–4191.

(62) Balık, M.; Bulut, V.; Erdogan, I. Y. Optical, Structural and Phase Transition Properties of Cu_2O, CuO and Cu_2O/CuO: Their Photoelectrochemical Sensor Applications. *Int. J. Hydrogen Energy* **2019**, *44* (34), 18744–18755.

(63) Rajesh, K. R.; Menon, C. S. Electrical and Optical Properties of Vacuum Deposited MnPc Thin Films. *Eur. Phys. J. B* **2005**, *47* (2), 171–176.

(64) Abass, A. K.; Krier, A.; Collins, R. A. The Influence of Iodine on the Electrical Properties of Lead Phthalocyanine (PbPC) Interdigital Planar Gas Sensors. *Phys. status solidi* **1994**, *142* (2), 435–442.

(65) Wang, H.; Xu, J.-Z.; Zhu, J.-J.; Chen, H.-Y. Preparation of CuO Nanoparticles by Microwave Irradiation. *J. Cryst. Growth* **2002**, *244* (1), 88–94.

(66) Yang, J.; Meldrum, F. C.; Fendler, J. H. Epitaxial Growth of Size-Quantized Cadmium Sulfide Crystals Under Arachidic Acid Monolayers. *J. Phys. Chem.* **1995**, *99* (15), 5500–5504.

(67) Dhineshbabu, N. R.; Rajendran, V.; Nithyavathy, N.; Vetumperumal, R. Study of Structural and Optical Properties of Cupric Oxide Nanoparticles. *Appl. Nanosci.* **2016**, *6* (6), 933–939.

(68) Sawicka-Chudy, P.; Sibiński, M.; Pawełek, R.; Wisz, G.; Cieniek, B.; Potera, P.; Szczepan, P.; Adamiak, S.; Cholewa, M.; Głowa, Ł. Characteristics of TiO_2, Cu_2O, and TiO_2/Cu_2O Thin Films for Application in PV Devices. *AIP Adv.* **2019**, *9* (5), 055206.

(69) Wooten, F. Optical Properties of Solids. Academic Press **1972**.

(70) Balamurugan, B.; Aruna, I.; Mehta, B. R.; Shivaprasad, S. M. Size-Dependent Conductivity-Type Inversion in Cu_2O Nanoparticles. *Phys. Rev. B* **2004**, *69* (16), 165419.

(71) Law, C. K. Resonance Response of the Quantum Vacuum to an Oscillating Boundary. *Phys. Rev. Lett.* **1994**, *73* (14), 1931–1934.

(72) Rakhshani, A. E. Preparation, Characteristics and Photovoltaic Properties of Cuprous Oxide—a Review. *Solid. State. Electron.* **1986**, *29* (1), 7–17.

(73) Gurlo, A. Interplay between O_2 and SnO_2: Oxygen Ionosorption and Spectroscopic Evidence for Adsorbed Oxygen. *ChemPhysChem* **2006**, *7* (10), 2041–2052.

(74) Barsan, N.; Weimar, U. Conduction Model of Metal Oxide Gas Sensors. *J. Electroceramics* **2001**, *7* (3), 143–167.

(75) Choi, S.-W.; Katoch, A.; Kim, J.-H.; Kim, S. S. Remarkable Improvement of Gas-Sensing Abilities in p-Type Oxide Nanowires by Local Modification of the Hole-Accumulation Layer. *ACS Appl. Mater. Interfaces* **2015**, *7* (1), 647–652.

(76) Hübner, M.; Simion, C. E.; Tomescu-Stănoiu, A.; Pokhrel, S.; Bârsan, N.; Weimar, U. Influence of Humidity on CO Sensing with P-Type CuO Thick Film Gas Sensors. *Sensors Actuators B Chem.* **2011**, *153* (2), 347–353.

(77) Lupan, O.; Postica, V.; Ababii, N.; Hoppe, M.; Cretu, V.; Tiginyanu, I.; Sontea, V.; Pauporté, T.; Viana, B.; Adelung, R. Influence of CuO Nanostructures Morphology on Hydrogen Gas Sensing Performances. *Microelectron. Eng.* **2016**, *164*, 63–70.

(78) Kim, H.-J.; Lee, J.-H. Highly Sensitive and Selective Gas Sensors Using P-Type Oxide

Semiconductors: Overview. *Sensors Actuators B Chem.* **2014**, *192*, 607–627.

(79)   Kamble, V. B.; Umarji, A. M. Gas Sensing Response Analysis of P-Type Porous Chromium Oxide Thin Films. *J. Mater. Chem. C* **2013**, *1* (48), 8167.

(80)   Choi, Y.-H.; Kim, D.-H.; Hong, S.-H.; Hong, K. S. H_2 and C_2H_5OH Sensing Characteristics of Mesoporous P-Type CuO Films Prepared via a Novel Precursor-Based Ink Solution Route. *Sensors Actuators B Chem.* **2013**, *178*, 395–403.

(81)   Lupan, O.; Postica, V.; Cretu, V.; Wolff, N.; Duppel, V.; Kienle, L.; Adelung, R. Single and Networked CuO Nanowires for Highly Sensitive P-Type Semiconductor Gas Sensor Applications. *Phys. status solidi - Rapid Res. Lett.* **2016**, *10* (3), 260–266.

(82)   Lupan, O.; Cretu, V.; Postica, V.; Polonskyi, O.; Ababii, N.; Schütt, F.; Kaidas, V.; Faupel, F.; Adelung, R. Non-Planar Nanoscale p–p Heterojunctions Formation in $Zn_xCu_{1-x}O_y$ Nanocrystals by Mixed Phases for Enhanced Sensors. *Sensors Actuators B Chem.* **2016**, *230*, 832–843.

(83)   Zappa, D.; Galstyan, V.; Kaur, N.; Munasinghe Arachchige, H. M. M.; Sisman, O.; Comini, E. "Metal Oxide -Based Heterostructures for Gas Sensors"- A Review. *Anal. Chim. Acta* **2018**, *1039*, 1–23.

(84)   Barsan, N.; Schweizer-Berberich, M.; Göpel, W. Fundamental and Practical Aspects in the Design of Nanoscaled SnO_2 Gas Sensors: A Status Report. *Fresenius. J. Anal. Chem.* **1999**, *365* (4), 287–304.

(85)   Zoolfakar, A. S.; Ahmad, M. Z.; Rani, R. A.; Ou, J. Z.; Balendhran, S.; Zhuiykov, S.; Latham, K.; Wlodarski, W.; Kalantar-zadeh, K. Nanostructured Copper Oxides as Ethanol Vapour Sensors. *Sensors Actuators B Chem.* **2013**, *185*, 620–627.

(86)   Hoppe, M.; Ababii, N.; Postica, V.; Lupan, O.; Polonskyi, O.; Schütt, F.; Kaps, S.; Sukhodub, L. F.; Sontea, V.; Strunskus, T.; Faupel, F.; Adelung, R. (CuO-Cu_2O)/ZnO:Al Heterojunctions for Volatile Organic Compound Detection. *Sensors Actuators B Chem.* **2018**, *255*, 1362–1375.

(87)   Lee, H.-J.; Jeong, S.-Y.; Cho, C. R.; Park, C. H. Study of Diluted Magnetic Semiconductor: Co-Doped ZnO. *Appl. Phys. Lett.* **2002**, *81* (21), 4020–4022.

(88)   Siemons, M.; Simon, U. Preparation and Gas Sensing Properties of Nanocrystalline La-Doped $CoTiO_3$. *Sensors Actuators B Chem.* **2006**, *120* (1), 110–118.

(89)   Mattsson, A.; Österlund, L. Adsorption and Photoinduced Decomposition of Acetone and Acetic Acid on Anatase, Brookite, and Rutile TiO_2 Nanoparticles. *J. Phys. Chem. C* **2010**, *114* (33), 14121–14132.

(90)   Morgan, B. J.; Watson, G. W. Intrinsic N-Type Defect Formation in TiO_2: A Comparison of Rutile and Anatase from GGA+ U Calculations. *J. Phys. Chem. C* **2010**, *114* (5), 2321–2328.

(91)   Lenaerts, S.; Roggen, J.; Maes, G. FT-IR Characterization of Tin Dioxide Gas Sensor Materials under Working Conditions. *Spectrochim. Acta Part A Mol. Biomol. Spectrosc.* **1995**, *51* (5), 883–894.

(92)   Chang, S. Oxygen Chemisorption on Tin Oxide: Correlation between Electrical Conductivity and EPR Measurements. *J. Vac. Sci. Technol.* **1980**, *17* (1), 366–369.

(93) Yamazoe, N.; Fuchigami, J.; Kishikawa, M.; Seiyama, T. Interactions of Tin Oxide Surface with O_2, H_2O AND H_2. *Surf. Sci.* **1979**, *86*, 335–344.

(94) Zhang, Y.-B.; Yin, J.; Li, L.; Zhang, L.-X.; Bie, L.-J. Enhanced Ethanol Gas-Sensing Properties of Flower-like p-CuO/n-ZnO Heterojunction Nanorods. *Sensors Actuators B Chem.* **2014**, *202*, 500–507.

(95) Sahay, P. P.; Tewari, S.; Jha, S.; Shamsuddin, M. Sprayed ZnO Thin Films for Ethanol Sensors. *J. Mater. Sci.* **2005**, *40* (18), 4791–4793.

(96) Hwang, I.-S.; Choi, J.-K.; Kim, S.-J.; Dong, K.-Y.; Kwon, J.-H.; Ju, B.-K.; Lee, J.-H. Enhanced H_2S Sensing Characteristics of SnO_2 Nanowires Functionalized with CuO. *Sensors Actuators B Chem.* **2009**, *142* (1), 105–110.

(97) Chen, Y.; Yu, L.; Feng, D.; Zhuo, M.; Zhang, M.; Zhang, E.; Xu, Z.; Li, Q.; Wang, T. Superior Ethanol-Sensing Properties Based on Ni-Doped SnO_2 p–n Heterojunction Hollow Spheres. *Sensors Actuators B Chem.* **2012**, *166–167*, 61–67.

(98) Liu, L.; Li, S.; Zhuang, J.; Wang, L.; Zhang, J.; Li, H.; Liu, Z.; Han, Y.; Jiang, X.; Zhang, P. Improved Selective Acetone Sensing Properties of Co-Doped ZnO Nanofibers by Electrospinning. *Sensors Actuators B Chem.* **2011**, *155* (2), 782–788.

(99) Lupan, O.; Postica, V.; Gröttrup, J.; Mishra, A. K.; de Leeuw, N. H.; Carreira, J. F. C.; Rodrigues, J.; Ben Sedrine, N.; Correia, M. R.; Monteiro, T.; Cretu, V.; Tiginyanu, I.; Smazna, D.; Mishra, Y. K.; Adelung, R. Hybridization of Zinc Oxide Tetrapods for Selective Gas Sensing Applications. *ACS Appl. Mater. Interfaces* **2017**, *9* (4), 4084–4099.

(100) Katoch, A.; Choi, S.-W.; Kim, H. W.; Kim, S. S. Highly Sensitive and Selective H_2 Sensing by ZnO Nanofibers and the Underlying Sensing Mechanism. *J. Hazard. Mater.* **2015**, *286*, 229–235.

(101) Lupan, O.; Postica, V.; Labat, F.; Ciofini, I.; Pauporté, T.; Adelung, R. Ultra-Sensitive and Selective Hydrogen Nanosensor with Fast Response at Room Temperature Based on a Single Pd/ZnO Nanowire. *Sensors Actuators B Chem.* **2018**, *254*, 1259–1270.

(102) Foo, M. L.; Huang, Q.; Lynn, J. W.; Lee, W. L.; Klimczuk, T.; Hagemann, I. S.; Ong, N. P.; Cava, R. J. Synthesis, Structure and Physical Properties of Ru Ferrites: BaMRu$_5$O$_{11}$ (M=Li and Cu) and BaM'_2Ru$_4$O$_{11}$ (M'=Mn, Fe and Co). *J. Solid State Chem.* **2006**, *179* (2), 563–572.

(103) Downie, L. J.; Black, C.; Ardashnikova, E. I.; Tang, C. C.; Vasiliev, A. N.; Golovanov, A. N.; Berdonosov, P. S.; Dolgikh, V. A.; Lightfoot, P. Structural Phase Transitions in the Kagome Lattice Based Materials Cs$_{2-X}$Rb$_x$SnCu$_3$F$_{12}$ (x = 0, 0.5, 1.0, 1.5). *CrystEngComm* **2014**, *16* (32), 7419–7425.

(104) Leinekugel-le-Cocq-Errien, A. Y.; Deniard, P.; Jobic, S.; Gautier, E.; Evain, M.; Aubin, V.; Bart, F. Structural Characterization of the Hollandite Host Lattice for the Confinement of Radioactive Cesium: Quantification of the Amorphous Phase Taking into Account the Incommensurate Modulated Character of the Crystallized Part. *J. Solid State Chem.* **2007**, *180* (1), 322–330.

(105) Hu, J.; Li, D.; Lu, J. G.; Wu, R. Effects on Electronic Properties of Molecule Adsorption on CuO Surfaces and Nanowires. *J. Phys. Chem. C* **2010**, *114* (40), 17120–17126.

(106) Wu, D.; Zhang, Q.; Tao, M. LSDA+U Study of Cupric Oxide: Electronic Structure and

Native Point Defects. *Phys. Rev. B* **2006**, *73* (23), 235206–235212.

(107) Forsyth, J. B.; Brown, P. J.; Wanklyn, B. M. Magnetism in Cupric Oxide. *J. Phys. C Solid State Phys.* **1988**, *21* (15), 2917–2929.

(108) Yang, B. X.; Tranquada, J. M.; Shirane, G. Neutron Scattering Studies of the Magnetic Structure of Cupric Oxide. *Phys. Rev. B* **1988**, *38* (1), 174–178.

(109) Ray, S. C. Preparation of Copper Oxide Thin Film by the Sol–Gel-like Dip Technique and Study of Their Structural and Optical Properties. *Sol. Energy Mater. Sol. Cells* **2001**, *68* (3–4), 307–312.

(110) Ghijsen, J.; Tjeng, L. H.; van Elp, J.; Eskes, H.; Westerink, J.; Sawatzky, G. A.; Czyzyk, M. T. Electronic Structure of Cu_2O and CuO. *Phys. Rev. B* **1988**, *38* (16), 11322–11330.

(111) HARDEE, K. L.; BARD, A. J. ChemInform Abstract: SEMICONDUCTOR ELECTRODES. X. PHOTOELECTROCHEMICAL BEHAVIOR OF SEVERAL POLYCRYSTALLINE METAL OXIDE ELECTRODES IN AQUEOUS SOLUTIONS. *Chem. Informationsd.* **1977**, *8* (20).

(112) Marabelli, F.; Parravicini, G. B.; Salghetti-Drioli, F. Optical Gap of CuO. *Phys. Rev. B* **1995**, *52* (3), 1433–1436.

(113) Osterloh, F. E. Inorganic Materials as Catalysts for Photochemical Splitting of Water. *Chem. Mater.* **2008**, *20* (1), 35–54.

(114) Nowotny, J.; Sorrell, C. C.; Bak, T.; Sheppard, L. R. Solar-Hydrogen: Unresolved Problems in Solid-State Science. *Sol. Energy* **2005**, *78* (5), 593–602.

(115) Bak, T.; Nowotny, J.; Rekas, M.; Sorrell, C. . Photo-Electrochemical Hydrogen Generation from Water Using Solar Energy. Materials-Related Aspects. *Int. J. Hydrogen Energy* **2002**, *27* (10), 991–1022.

(116) FUJISHIMA, A.; HONDA, K. Electrochemical Photolysis of Water at a Semiconductor Electrode. *Nature* **1972**, *238* (5358), 37–38.

(117) Henkelman, G.; Arnaldsson, A.; Jónsson, H. A Fast and Robust Algorithm for Bader Decomposition of Charge Density. *Comput. Mater. Sci.* **2006**, *36* (3), 354–360.

(118) Sanville, E.; Kenny, S. D.; Smith, R.; Henkelman, G. Improved Grid-Based Algorithm for Bader Charge Allocation. *J. Comput. Chem.* **2007**, *28* (5), 899–908.

(119) Tang, W.; Sanville, E.; Henkelman, G. A Grid-Based Bader Analysis Algorithm without Lattice Bias. *J. Phys. Condens. Matter* **2009**, *21* (8), 084204.

(120) Roldan, A.; Santos-Carballal, D.; de Leeuw, N. H. A Comparative DFT Study of the Mechanical and Electronic Properties of Greigite Fe_3S_4 and Magnetite Fe_3O_4. *J. Chem. Phys.* **2013**, *138* (20), 204712.

(121) Santos-Carballal, D.; Roldan, A.; Grau-Crespo, R.; de Leeuw, N. H. A DFT Study of the Structures, Stabilities and Redox Behaviour of the Major Surfaces of Magnetite Fe_3O_4. *Phys. Chem. Chem. Phys.* **2014**, *16* (39), 21082–21097.

(122) Santos-Carballal, D.; Roldan, A.; Grau-Crespo, R.; de Leeuw, N. H. First-Principles Study of the Inversion Thermodynamics and Electronic Structure of FeM_2X_4 (Thio)Spinels (M = Cr, Mn, Co, Ni; X = O, S). *Phys. Rev. B* **2015**, *91* (19), 195106.

(123) Santos-Carballal, D.; Roldan, A.; de Leeuw, N. H. Early Oxidation Processes on the Greigite Fe_3S_4(001) Surface by Water: A Density Functional Theory Study. *J. Phys. Chem. C* **2016**, *120* (16), 8616–8629.

(124) Santos-Carballal, D.; Roldan, A.; Dzade, N. Y.; de Leeuw, N. H. Reactivity of CO_2 on the Surfaces of Magnetite (Fe_3O_4), Greigite (Fe_3S_4) and Mackinawite (FeS). *Philos. Trans. R. Soc. A Math. Phys. Eng. Sci.* **2018**, *376* (2110), 20170065.

(125) Santos-Carballal, D.; Roldan, A.; De Leeuw, N. H. CO_2 Reduction to Acetic Acid on the Greigite Fe_3S_4 {111} Surface. *Faraday Discuss.* **2020**.

(126) Wiberg, K. B.; Rablen, P. R. Comparison of Atomic Charges Derived via Different Procedures. *J. Comput. Chem.* **1993**, *14* (12), 1504–1518.

(127) Ángyán, J. G.; Jansen, G.; Loss, M.; Hättig, C.; Heß, B. A. Distributed Polarizabilities Using the Topological Theory of Atoms in Molecules. *Chem. Phys. Lett.* **1994**, *219* (3–4), 267–273.

(128) De Proft, F.; Van Alsenoy, C.; Peeters, A.; Langenaeker, W.; Geerlings, P. Atomic Charges, Dipole Moments, and Fukui Functions Using the Hirshfeld Partitioning of the Electron Density. *J. Comput. Chem.* **2002**, *23* (12), 1198–1209.

(129) Coey, J. M. D.; Venkatesan, M. Half-Metallic Ferromagnetism: Example of CrO_2 (Invited). *J. Appl. Phys.* **2002**, *91* (10), 8345–8350.

(130) Coey, J. M. D.; Chien, C. L. Half-Metallic Ferromagnetic Oxides. *MRS Bull.* **2011**, *28* (10), 720–724.

(131) Coey, J. M. D.; Venkatesan, M.; Bari, M. A. Half-Metallic Ferromagnets. In *High Magnetic Fields. Lecture Notes in Physics, Vol. 595*; Berthier, C., Levy, L. P., Martinez, G., Eds.; Springer Berlin Heidelberg, **2001**; pp 377–396.

(132) Coey, J. M. D.; Sanvito, S. Magnetic Semiconductors and Half-Metals. *J. Phys. D. Appl. Phys.* **2004**, *37* (7), 988–993.